Long-term evolution of surf zone sand bars: the effect of the surface rollers

MPOC Master thesis

Konstantinos Chasapis Tassinis

Supervised by:
Prof. dr. Huib E. de Swart
dr. Carles Panades Guinart

Institute for Marine and Atmospheric research Utrecht (IMAU)
Utrecht, the Netherlands

Front cover picture taken from Short (1999).

Abstract

A variety of different bed forms is observed in the nearshore zone of coastal seas. Gaining knowledge on the evolution of the morphology of such sytems is important for engineering purposes, preservation of coastal systems and to increase public awereness for the transitional states of the beaches. In this study, the effect of the rollers, which form during wave breaking, on the long term evolution of the bed patterns is investigated. The surface roller is the aerated mass of water located on the shoreward face of the breaking waves. The working hypothesis of the present study is that additional physics results in new bottom patterns such as shoreline sand bars.

The specific objectives of this study are threefold. First, to quantify the changes in the behaviour of the variables of the basic state (representing longshore averaged conditions) when rollers are included in the system. Second, to analyze the spatio-temporal characteristics of the growing crescentic bars in the initial stages of their formation. Third, to investigate the effect of the rollers on the growth, position, shape and flow characteristics of the bed features in the finite amplitude regime. In order to answer these questions the nonlinear system of equations that describe the waves, the rollers and the currents coupled with the sediment transport and the bed evolution equations is solved by the numerical model Morfo55+. Compared to a case without the rollers, for the basic state, the results show that when including the rollers in the model the set-up is smaller in the inner surf zone. The depth-integrated concentration maxima are shifted shoreward of the longshore sand bar compared to the case without the rollers. Moreover, for the initially forming sand bars, it is found that when rollers are activated, their growth is slower than the roller-off case. Results obtained from Morfo55+ and the results provided by linear stability analysis (Morfo62) show that the difference in the e-folding time between the two models is less than 5% with rollers. However, for the roller-off case the difference is almost 50%. With Morfo55+ the linear regime ends after $\simeq 2$ days, when rollers are activated. For the roller-off case nonlinear effects are evident after $\simeq 1.7$ days. For the nonlinear regime, between the two cases, bars are different in growth rates, wavelengths and maximum amplitudes. The most important result is that sand-bars form close to the shoreline only when the rollers are included in the model. Further analysis, showed that the inclusion of the rollers both in the hydrodynamics and the sediment transport is needed for shoreline sand bars to occur.

Contents

Chapter 1

Introduction

Coastal areas around the world are often characterized by sandy beds bordered by long beaches. Such areas are found in the east coast of Australia and of the USA, as well as in the western coast of the Netherlands and the Atlantic coast of France. The study of the evolution of nearshore morphological systems is directly linked to societal, engineering and scientific purposes. Gaining knowledge on their long-term evolution can be very useful for coastal infrastucture safety and natural environment preservation. Moreover, modeling the evolution of these beach systems is very impotant when humans intervene in several ways. This involves from extracting/adding sand to installation of large machinery in the coasts, such as underwater energy turbines.

The present study predominantly focuses in the shoaling zone and the surf zone, which are shown in the conceptual picture of Fig.(1.1), bounded by a vertical wall at the shoreline. In this region, the approaching waves are transformed due to the reducing depth, grow in amplitude and eventually break.

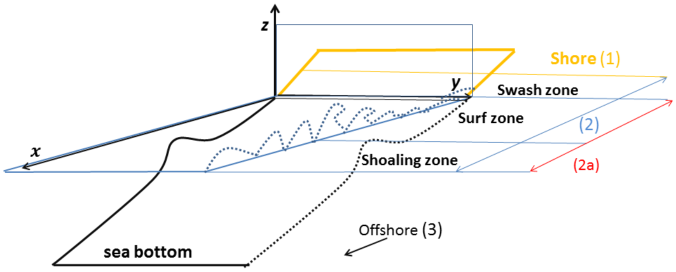

Figure 1.1: Conceptual picture of the coastal area with a sloping bottom and a single longshore uniform sand bar. Numbers indicate the different areas: shore (1), nearshore (2), study area of this study (2a), offshore (3). Approaching waves are also scetched.

Frequently, the morphology of the coastal seas shows various bed forms that are rhythmic. A classification of the different beach states and the different sand bar types has been made by Wright & Short (1984). Some of them are: transverse bars, crescentic bars and ridge and runnel systems (Fig.(1.2) a, c). In this figure, the intensity of the image is used to indentify where most of the wave breaking occurs. In turn, the breaking waves indicate the presence of the shallows, i.e. bathymetric anomalies, which in these cases are rhythmic. Crescentic bars span in the order of hundreds meters along the beach and they are separated by bed depressions in between, called rip channels. They are linked to the presence of initially longshore uniform bars, which form during storms. Crescentic bars usually evolve under post-storm wave conditions in time scales of a few days (Van Enckevort et al, 2004). An example of such patterns is shown in Fig.(1.2c): over the shore parallel sand bar (white line in the right) bed patterns that resemble crescentic moons are observed.

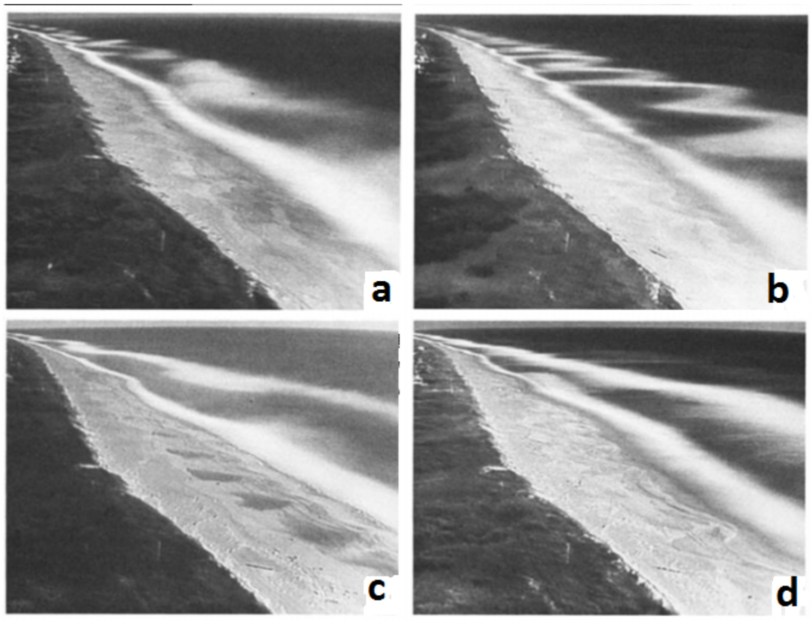

Figure 1.2: 10-minute time exposure images showing different kinds of bed patterns: a) transverse bars b) transverse bars with different wavelength c) crescentic bars d) longshore uniform sand bar. The increased white foam due to the breaking waves in the surf zone indicates the presence of the shoals. Picture taken from Lippmann & Holman (1990)

A well established theory that explains the formation of such bed forms is the self organization mechanism (Falques et al, 2000, Calvete et al., 2005 and references herein). According to this, bed patterns grow due the positive feedback between the morphology and the hydrodynamics. If an initial bottom profile is in equilibrium, then a small topographic perturbation, superimposed on the bottom will modify the waves and the currents which will subsequently affect the sediment transport. The divergence or convergence of the latter will either reinforce or damp the perturbation and thus the bed will grow or decay.

Crescentic bars form in the case of normally, or near normally, incident waves to the shoreline, i.e. in the absence of a longshore current. This study considers only such waves. Past studies (Falques et al., 2000), have linked the formation of crescentic bar systems with a cellular circulation pattern and the spatial distribution of the stirring of sediment caused by the waves. In particular, increased wave breaking over the crests, leads to longshore variations of set up, that drives a certain cellular circulation. The currents transport the sediment that is accumulated reinforcing the shoals, thus leading to a positive feedback mechanism.

Recently, an additional physical process, the surface rollers, has been added in several models (Reniers et al., 2004; Ribas et al., 2011), describing a more realistic picture of the breaking waves. Physically, the roller is the aerated mass in the shoreward face of the breaking wave. In the model, the inclusion of the rollers affects both the currents and the sediment transport. The energy that is lost by wave breaking is temporarily stored in the rollers and then is dissipated. The roller energy gives rise to roller radiation stresses the divergence of which creates an additional force to drive the currents. Additionally, the bed shear stress exerted by the currents and the orbital motion of waves at the bottom is increased due to resuspension of sediment by the rollers. So far, these processes have been investigated in studies that were only able to describe the initial formation of bars, for either normal or oblique incident waves. Ribas et al. (2011) have investigated the role of the surface rollers in both the hydrodynamics and the sediment transport in the initial formation of transverse finger bars. They found, after comparison of model results with characteristics of observed transverse bars at the Noordwijk beach, the Netherlands, that the inclusion of rollers is necessary to describe accurately their wavelength, crest orientation and e-folding growth time. Also, according to their results, positive feedback between the bed and the flow that gives rise to transverse bars, only occurs when resuspension of sediment due to the rollers is included in the sediment transport. Furthermore, in Ribas et al. (2012), the model results showed that the characteristics of crescentic bars are more accurate (compared with real time data from the Noordwijk beach), if the longshore current is simulated with the presence of the rollers. Both studies used models which employed linear stability analysis. This implies that only the initial formation of the patterns has been simulated and that finite-amplitude effects have been omitted. Garnier et al. (2008) have used a fully nonlinear model to simulate the long-term evolution of sand bars for both normally and obliquely incident waves. In that study, results of bed forms were analyzed for up to 100 days of morphological evolution. In the finite-amplitude regime, saturation of growth was obtained for the crescentic bar system, meaning that bars hardly grew after $\simeq 20$ days of morphological evolution. The system went trough several transitions and was in agreement with conceptual models of other studies (Wright & Short, 1984). Castelle et al. (2012) have also made extended simulations (in the order of tenths of days), inspecting the role of a bathymetric anomaly on the wavelength, growth rate and migration rate of rip channel systems. Their analysis showed that, downdrift of the anomaly, rip channels self-organize into patterns with larger wavelengths and smaller migration rates compared to the ones updrift. However, both studies did not include the surface rollers.

The working hypothesis of this project is that roller processes are going to resolve bed patterns in the long-term that - so far- morphodynamic models have not shown, either because only the initial formation of the bed forms has been described or because the long-term simulations did not include the rollers. In particular, it is aimed to show that shoreline undulations are going to form only with the present configuration. Although crescentic bars are nowadays well understood (Caballeria et al., 2001 and Calvete el al., 2005), there is a lack of long-term simulations with a fully nonlinear model that includes the rollers. Evidently, the joint action of and between physical processes at various time and length scales in the surf zone, still makes the analysis of such systems a prominent task.

The research questions about the evolution of the sand-bars under the effect of the surface rollers are the following:

1. What are the differences in the wave and roller energy, mean sea level and integrated concentration between the default case (rollers activated) and a roller-off case in the case of an initially alongshore uniform beach?
2. What are characteristics of bars (growth rate, amplitude, wavelength) that initially form in the surf zone, in the default case and the roller-off case?
3. What are the time limits of the linear regime? What is the effect of the rollers on the growth rate, amplitude, wavelength and position of the sand-bars in the finite-amplitude regime?

How the morphology of the surf zone is directly related to the currents and the waves? The flow chart of the feedback between the different components is depicted in Fig.(1.3). The breaking waves in the surf zone and the induced currents are eroding the bed and transport sediment, respectively, the divergence of which determines the evolution of the bed. Subsequently, the updated bottom profile affects the waves and the currents. Note that, the induced currents also interact with the waves. To address the 3 research questions, experiments are conducted with a numerical model. In particular, an extension of the existing Morfo55 model (Garnier, 2006) is used that includes surface rollers. Throughout this study, experiments are carried out with two configurations: one that includes all roller dynamics (default case) and one that does not. The model results are then analyzed and compared between these two cases, in order to quantify the differences in the sand bar characteristics.

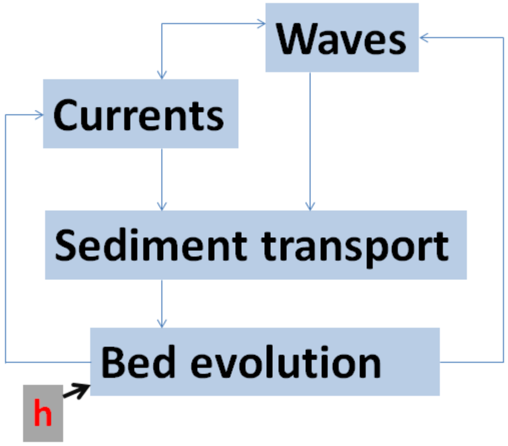

Figure 1.3: Schematic picture of the different components and the feedbacks.

The remainder of this M.Sc. thesis is structured as follows. In Chapter 2 the equations of the morphodynamical model are presented. The model consists of equations for the waves and the currents that are coupled with equations for the sediment transport and the bed evolution. Moreover, some basics on linear stability analysis are provided. In Chapter 3 the experimental setup and the methodology are described. The parameters, their values and their meaning for the so-called default case are explained. Then, the methods to analyze results and answer the three research questions follow. In Chapter 4 the results for the basic state and the initial formation of bars are presented, thereby answering question 1 and 2. In Chapter 5 the results for the finite-amplitude regime are given, associated with question 3. Furthermore, Chapter 6 discusses some physical mechanisms that provide an explanation for the effect of the rollers on two of the most important results, namely the formation of sand bars at the shoreline and the decrease of the global growth rate. Also, some information is given on the limitations of the model. In Chapter 7 conclusions are drawn.

Chapter 2

Material

In this chapter, a description of the material that is used in this study is given. Two numerical models are employed in order to obtain and analyze results: the Morfo55 (Garnier, 2006) and the Morfo62 model (Calvete et al., 2005, Ribas, 2003). The former is the main tool for this study and is used in every experiment that is performed. The latter is an assistant tool that aids in testing the performance of Morfo55. Section (2.1) describes the updated version of the Morfo55 model, which includes the surface rollers and Section (2.2) briefly presents the Morfo62 model and linear stability analysis.

2.1 The Morfo55+ model

2.1.1 Introduction

The present model is an extension of the nonlinear model Morfo55 (from now on Morfo55+) and it has been modified in order to include surface rollers. These modifications have been implemented in the model with three main options that can be "switched on and off" separately so that it can run with or without them (see Subsection (2.1.6) for an overview of these options).

In general, Morfo55+ is a nonlinear model that numerically solves the depth-averaged shallow water equations coupled with the sediment transport and the bed evolution equations. It can be described as a surf zone model based on the fact that it simulates the self-organized processes that generate the morphodynamical instabilities in the surf zone. These self-organized processes occur due to the feedbacks between the waves, the rollers, the depth averaged currents and the bed evolution (Ribas et al., 2011).

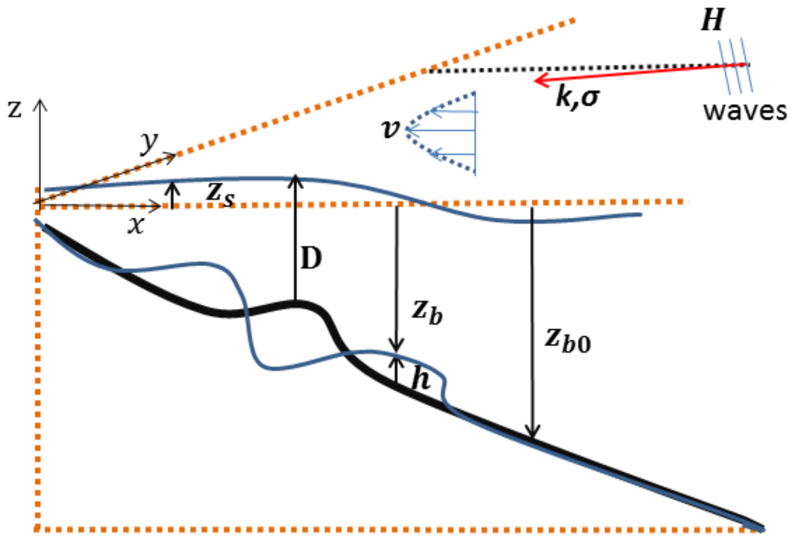

Figure 2.1: Physical domain and unknown variables of the physical system

2.1.2 Physical domain

The physical domain consists of a coordinate system $(0, x, y, z)$ or $(0, x_1, x_2, x_3)$ with an erodible bottom profile that can be subjected to morphological changes under the influence of sediment transport (Fig.(2.1). The longshore direction $[0, y)$ coincides with a rectilinear shoreline, the positive cross-shore direction $[0, x)$ points at the seaward direction and the positive vertical direction $[0, z)$ points upwards.

Fig.(2.1) shows the variables for the waves, the currents and the morphology. Wave and depth averaged properties of the original instantaneous variables are considered. Wave averaging stands for mean variables over the wave period T and depth averaging means that the variables are depth uniform. In the surf zone, shallow water theory is employed (Mei 1989). The coordinate system after averaging is $(0, x_1, x_2, t)$. The figure shows:

- ▷ the properties of the waves: the wave vector $\mathbf{k}(x_1 x_2, t)$, the wave frequency $\sigma(x_1, x_2, t)$ and the wave height $H\,(x_1, x_2, t))$,

- ▷ the properties of the currents: the wave and depth averaged horizontal velocity vector $\boldsymbol{v}(x_1 x_2, t)$, where $\boldsymbol{v} = (u, v) = (v_1, v_2)$,
- ▷ the sea level and the properties of the bed: the wave averaged free sea level $z_s(x_1, x_2, t)$, the wave averaged bed level $z_b(x_1, x_2, t)$, the wave averaged bed pertubation $h(x_1, x_2, t)$ and finally the wave averaged depth $D(x_1, x_2, t) = z_s(x_1, x_2, t) - z_b(x_1, x_2, t)$.

2.1.3 Hydrodynamics

2.1.3.1 Waves

In the present study, surface gravity waves are considered that originate from deep water and travel to the coast. Breaking waves in the surf zone induce a subsequent circulation by transferring momentum into the water. Waves are considered to be irregular with random wave heights H, with a spectrum that is narrow in frequency and angle. These heights H follow the Rayleigh distribution, from which the root mean square wave height H_{rms} and the wave energy density $E = \rho g H_{rms}^2/8$ can be computed , with ρ being the water density and g the acceleration due to gravity.

As the waves approach the coast, linear wave theory is used to physically describe a number of properties such as the intrinsic wave frequency σ, i.e. as experienced by an observer moving with the current

$$\sigma = \sqrt{g \mathrm{k} \tanh(\mathrm{k} D)} \,, \tag{2.1}$$

where k is the module of the wavenumber vector $\mathbf{k} = (\mathrm{k}_1, \mathrm{k}_2)$. The phase velocity is defined as

$$c = \frac{\sigma}{\mathrm{k}} = \sqrt{\frac{g}{\mathrm{k}} \tanh(\mathrm{k} D)} \tag{2.2}$$

whose components are straightforwardly computed via

$$c_i = \frac{k_i}{k} c \, \text{for} \; i = 1, 2 \,. \tag{2.3}$$

Similarly, the components of the group velocity $\mathbf{c_g}$ are

$$c_{gi} = \frac{k_i}{k} c_g, \quad i = 1, 2 \tag{2.4}$$

and its magnitude is calculated by means of

$$c_g = \frac{\partial \sigma}{\partial k} = \frac{c}{2} \left(1 + \frac{2kD}{\sinh(2kD)} \right) \,. \tag{2.5}$$

Lastly, the root mean square velocity u_{rms} of the waves is

$$u_{rms} = \frac{\sigma H_{rms}}{2 \sinh(kD)} \,, \tag{2.6}$$

where D is the water depth and k the modulus of the wavenumber. The Doppler shift is considered and the intrinsic frequency σ is related with the absolute frequency ω, i.e. the frequency experienced by an inertial observer. The relation reads,

$$\omega = \sqrt{gk \tanh{(kD)}} + v_i k_i, \quad i = 1, 2. \,, \tag{2.7}$$

with v_i representing the two components of the current velocity vector $\boldsymbol{v}$. Due to the irrotationality of the wavenumber,

$$\frac{\partial k_i}{\partial x_j} - \frac{\partial k_j}{\partial x_i} = 0, \quad i, j = 1, 2 \,, \tag{2.8}$$

Refraction of the waves is computed with the global Snell law, i.e.

$$k_i \sin\theta = k_i^{off} \sin\theta^{off} \tag{2.9}$$

where k^{off} and θ^{off} are the wavenumber and the angle of incidence of the wave far offshore, respectively. Equations (2.7) and (2.9) describe the mechanism of wave refraction. Other more complicated physical processes, like diffraction of waves due to vertical objects or islands will be considered to be beyond the scope of this study.

The wave energy balance, including wave-current interactions, reads,

$$\frac{\partial E}{\partial t} + \frac{\partial}{\partial x_j}\left(\left(v_j + c_{gj}\right) E\right) + S_{ij}^{w} \frac{\partial v_j}{\partial x_i} = -\mathcal{D}, \quad i, j = 1, 2 \,, \tag{2.10}$$

where v_j are the current velocity components in (x_1, x_2), S_{ij}^w are the wave radiation stresses and $\mathcal{D}$ is the dissipation rate due to the breaking of the waves and due to bottom friction. Therefore $\mathcal{D} = \mathcal{D}^w + \mathcal{D}^f$. The linear wave theory is used to formulate the expressions for the wave radiation stresses (Longuet-Higgins-Stewart, 1964) . It reads,

$$S_{ij}^{w} = E\left(\frac{c_g}{c}\frac{k_i k_j}{k^2} + \left(\frac{c_g}{c} - \frac{1}{2}\right)\delta_{ij}\right), \quad i, j - 1, 2 \,, \tag{2.11}$$

where $\delta_{ij}$is the Kronecker delta and c_g, c are the moduli of the group velocity and phase velocity, given by (2.4) and (2.1), respectively.

For the dissipation rate due to the breaking of the waves the formulation of Thornton & Guza (1983) is adopted

$$\mathcal{D}^{w} = \frac{3\sqrt{\pi}}{16} B^3 f_p \rho g \frac{H_{rms}^5}{\gamma_b D^3}\left(1 - \frac{1}{\left(1 + \left(H_{rms}/\gamma_b D\right)^2\right)^{5/2}}\right) \,, \tag{2.12}$$

Here $B = 1$ is the breaker index. In this case, the entire wave front is considered to be covered with foam. Moreover, γ_b is the index of wave saturation, given by H_{rms}/D, and f_p the intrinsic frequency peak of the wave field, $f_p = \sigma/2\pi$.The dissipation due to bottom friction $\mathcal{D}^f$ is parameterized according to Horikawa (1988),

$$\mathcal{D}^{f} = \frac{4}{3\pi}\rho C_D \frac{\pi^3 H_{rms}^3}{T^3}\frac{1}{\sinh^3{(kD)}} \,, \tag{2.13}$$

with C_D being the dimensionless drag friction coefficient $C_D = 5\ 10^{-3}$ and $T = 2\pi/\omega$ being the period of the waves. The energy dissipated by the breaking waves feeds the surface rollers, i.e. the aerated mass of water located on the shoreward face of the breaking waves. Following Reniers et al. (2004) and Ribas et al. (2011) the roller energy equation, including wave-current interactions, reads

$$\frac{\partial \left(2E^r\right)}{\partial t} + \frac{\partial}{\partial x_i}\left(2\left(v_i + c_i\right)E^r\right) + S^r_{ij}\frac{\partial v_j}{\partial x_i} = -\mathcal{D}^r + \mathcal{D}, \quad i,j = 1,2\,, \tag{2.14}$$

with E^r representing the roller energy density, c_i being the x_i − direction phase velocity components and S^r_{ij} being the radiation stresses due to roller propagation. The latter are parameterized, following Ribas et al. (2011)

$$S^r_{ij} = 2E^r\frac{k_i k_j}{|\boldsymbol{k}|^2}, \quad i,j = 1,2\ . \tag{2.15}$$

For the roller energy dissipation rate the formulation of Rueesink et al (2001) is adopted

$$\mathcal{D}^r = \frac{2gE^r \sin\left(\beta_{rol}\right)}{c}\,. \tag{2.16}$$

In this equation $\beta_{rol} = 0.1$ is the angle of the wave/roller interface.

2.1.3.2 Currents

Currents are physically described by conservation of water mass, i.e.

$$\frac{\partial D}{\partial t} + \frac{\partial}{\partial x_j}\left(Dv_j\right) = 0, \quad j = 1,2 \tag{2.17}$$

and the momentum balance equations,

$$\frac{\partial v_i}{\partial t} + v_j\frac{\partial v_i}{\partial x_j} = -g\frac{\partial z_s}{\partial x_i} + \frac{1}{\rho D}\frac{\partial}{\partial x_j}\left(S^w_{ij} + S^r_{ij} + S^t_{ij}\right) - \frac{\tau_{bi}}{\rho D}, \quad i,j = 1,2\,, \tag{2.18}$$

In equation (2.18), S^t_{ij} are the turbulent Reynolds stresses and τ_{bi} is the bottom shear stress. Wind stress and tidal forcing will not be accounted in the momentum balance and will be excluded from any further discussion. For the bottom shear stress the extension of the Feddersen et al. (2000) formulation for a 2-dimensional flow by Ribas et al. (2011) is chosen

$$\tau_{bi} = \rho c_D \frac{u_{rms}}{\sqrt{2}} v_i \left(1.16^2 + 2\frac{|\boldsymbol{v}|}{u^2_{rms}}\right)^{1/2}, \quad i = 1,2\ ,$$

with u_{rms} the root mean square velocity of the waves to the bottom and c_D being the dimensionless hydrodynamic drag coefficient of friction that follows the Manning-Stricker law (Soulsby, 1997)

$$c_D = 0.015\left(\frac{k_a}{D}\right)^{1/3}. \tag{2.19}$$

Here k_a is the apparent bed roughness (default value $k_a = 3.5 \cdot 10^{-2}$ m). Finally, the turbulent Reynolds stresses are described by

$$S^t_{ij} = \rho \nu_t D \left(\frac{\partial v_i}{\partial x_j} + \frac{\partial v_j}{\partial x_i} \right) , \quad i, j = 1, 2 \, , \tag{2.20}$$

with the lateral turbument mixing coefficient being

$$\nu_t = M \left(D^r / \rho \right)^{1/3} \ , \tag{2.21}$$

where M is a turbulence parameter equal to 1. When rollers are de-activated $D^r = D^w$ in this equation.

2.1.4 Bed Evolution and Sediment Transport

The hydrodynamic variables are coupled with the bed level z_b through the conservation of sediment mass

$$\frac{\partial z_b}{\partial t} + \frac{1}{1-p} \frac{\partial q_j}{\partial x_j} = 0, \quad j = 1, 2 \, , \tag{2.22}$$

which describes the evolution of the mean bed level $z_b(x_1, x_2, t)$, with $p = 0.4$, being the porosity (the ratio of 'empty' volume space over the total volume space between the grains of sediment) and q_j being the jth component of the wave averaged volumetric sediment transport vector $\boldsymbol{q}$ per unit width (m^{2}s^{-1}). Note that, according to equation (2.22), the evolution of the bed level z_b increases (accretion) if there is convergence of sediment. Similarly, if there is divergence of sediment (erosion), the bed level z_b decreases. Sediment transport $\boldsymbol{q} = (q_1, q_2)$ is computed following the total load sediment transport formula of Soulsby and Van Rijn (Soulsby, 1997). It reads

$$q_i = C \left(v_i - \Gamma \frac{\partial h}{\partial x_i} \right) , \quad i = 1, 2 \, . \tag{2.23}$$

Here, C can be interpreted as the depth integrated volumetric sediment concentration, often also called the stirring function, and Γ is the bed slope coefficient, which accounts for the tendency of the bed perturbations h to be smoothed out downslope. The depth integrated sediment concentration C follows

$$C = A_s \left(u_{stir} - u_{crit} \right)^{2.4} \quad \text{,if} \ \ u_{stir} > u_{crit} \tag{2.24}$$

$$C = 0 \qquad\qquad \text{,otherwise.} \tag{2.25}$$

In this expression $A_s = A_{ss} + A_{SB}$ is a constant that represents suspended and bedload sediment transport and that depends on the sediment characteristics and the water depth D. The term $u_{stir} - u_{crit}$ is the threshold for the current above which sediment is stirred and it also depends on sediment characteristics. The sediment coefficients read

$$A_{SS} = \frac{0.012 d_{50} D_*^{-0.6}}{\left(\left(s-1\right) g d_{50}\right)^{1.2}}\ , \tag{2.26}$$

$$A_{SB} = \frac{0.005 h \left(d_{50}/D\right)^{1.2}}{\left(\left(s-1\right) g d_{50}\right)^{1.2}}\ , \tag{2.27}$$

where d_{50} is the median grain size, $d_{50} = 0.20$ mm, s is the density of the sediment, $s = 2.65$, and D_* is the dimensionless grain size, given by

$$D_* = \left(\frac{g\left(s-1\right)}{\kappa_b^2}\right)^{1/3} d_{50}\ , \tag{2.28}$$

with κ_b being the kinematic viscosity of water ($\kappa_b = 1.3\ 10^{-6}\ \mathrm{m^2 s^{-2}}$). In equation (2.24) u_{crit} given by

$$u_{crit} = \Lambda \log_{10} \frac{h}{d_{50}}\ , \tag{2.29}$$

with

$$\Lambda = 0.19 \left(d_{50}\right)^{0.1} \ \ \text{for}\ \ 0.0001\ \mathrm{m} \leq d_{50} \leq 0.0005\ \mathrm{m}\,, \tag{2.30}$$

or

$$\Lambda = 8.5 \left(d_{50}\right)^{0.6} \ \ \text{for}\ \ 0.0005\ \mathrm{m} \leq d_{50} \leq 0.002\ \mathrm{m}\,.$$

The stirring velocity u_{stir} is the velocity representing resuspension of sediment and it reads

$$u_{stir} = \sqrt{|\boldsymbol{v}| + 0.018 c_D^{-1} u_{rms}^2 + n_{bor} u_{bor}^2} \tag{2.31}$$

with c_D , being the drag coefficient, given by expression (2.19).
In equation (2.31) n_{bor} is a constant parameter represents the turbulence velocity of the vortices after roller energy is dissipated (Calvete et al., 2011). Physically the last term in the rhs of equation (2.31) describes the stirring of sediment due to turbulence induced by the surface rollers. The velocity u_{bor} is related with the roller energy dissipation and is given by,

$$u_{bor}^2 = \left(\frac{\mathcal{D}^r}{\rho}\right)^{2/3} \left(\exp\left(\frac{D}{H_{rms}}\right) - 1\right)\ ,^{-1} \tag{2.32}$$

where the roller dissipation $\mathcal{D}^r$ is given by equation (2.16) and D is the mean depth. The exponential profile of u_{bor} accounts for the decrease of the turbulence velocity from the surface to the bottom of the physical domain. Of significant importance is the roller stirring parameter n_{bor}. By decreasing (increasing) n_{bor}, the resuspension of sediment due to the presence of the rollers is aslo decreased (increased) (see equation (2.31) & (2.32)). The original Soulsby-Van Rijn formulation (i.e. without surface rollers) is obtained for $n_{bor} = 0$. Therefore, the value of n_{bor} (being equal to 0 or not) determines to what extent the rollers account for stirring of sediment.
The bedslope coefficient $\mathit{\Gamma}$ in (2.23) is calculated as

$$\mathit{\Gamma} = \gamma \left(u_{stir} - u_{crit} \right) \,, \tag{2.33}$$

with u_{stir} given by equation (2.31) and γ being a constant, called the bed slope parameter.

2.1.5 Boundary Conditions

In order for the system presented in Subsections (2.1.3) - (2.1.4) to be mathematically well defined, boundary conditions for the unknown variables must be imposed. The unknown variables that need to be imposed to such conditions are $E, E^r, \boldsymbol{v}, D, z_b, z_s, \boldsymbol{q},$ and $\boldsymbol{k}$. Three types of boundaries should be defined: shoreline, offshore and lateral boundaries. The domain is L_x wide (x-direction) and L_y long ($y-$direction). The boundary conditions are similar to those explained by Caballeria et al. (2002) and Garnier (2006), except that extra conditions must be accounted for the roller dynamics.

2.1.5.1 Shoreline

At the shoreline a virtual vertical wall is considered, meaning that swash dynamics will be completely neglected from the scope of this study. This means that at the shore, $x_1 = 0$, the cross shore component of the velocity and of the sediment transport must vanish, i.e.

$$v_1(0, x_2, t) = 0 \,\text{and}\, \mathrm{q_1(0, x_2, t)} = 0 \,. \tag{2.34}$$

A no slip boundary condition is imposed and the longshore component of the velocity must also vanish at the shore,

$$v_2(0, x_2, t) = 0 \,. \tag{2.35}$$

Roller energy $E^r(0, x_2, t)$ and the rest of the variables are set to behave free according to the equations that describe them.

2.1.5.2 Offshore

At the boundary $x_1 = L_x$ it follows:

$$E^{off} = E(L_x, x_2, t) = \rho g \left(H_{rms}^{off} \right)^2 /8 \,. \tag{2.36}$$

Since the formation of bars in the surf zone will induce a currents that will be coupled with the growing bed patterns, extra boundary conditions must be accounted for, so that the induced flow still vanishes offshore. To that end, the following conditions are assigned,

$$\kappa_i \frac{\partial v_i}{\partial x_i} + v_i = 0, \quad i = 1, 2. \text{ at } x_1 = L_x \,, \tag{2.37}$$

with $\kappa_i > 0$ being constant coefficients describing an exponential decay of the flow in the offshore direction at this boundary.

2.1.5.3 Lateral

Periodic boundary conditions are imposed at the two lateral boundaries, i.e. at $x_2 = 0$ and $x_2 = L_y$, for $E, E^r, \boldsymbol{v}, z_b, z_s, D, \boldsymbol{k}$ and $\boldsymbol{q}$. As an example, the energy density E and the roller energy density E^r conditions read,

$$E(x_1, 0, t) = E(x_1, L_y, t)\,, \tag{2.38}$$

$$E^r(x_1, 0, t) = E^r(x_1, L_y, t)\,. \tag{2.39}$$

Also, periodic boundary conditions are applied to the first longshore derivatives of the unknown variables. Again, as an example, tthese conditions for E, E^r read,

$$\frac{\partial}{\partial x_2}\left(E(x_1, 0, t)\right) = \frac{\partial}{\partial x_2}\left(E(x_1, L_y, t)\right)\,, \tag{2.40}$$

$$\frac{\partial}{\partial x_2}\left(E^r(x_1, 0, t)\right) = \frac{\partial}{\partial x_2}\left(E^r(x_1, L_y, t)\right)\,. \tag{2.41}$$

2.1.6 Overview of model options

Overall, there are three ways of explicitly including rollers in the present model. These are summarized under three main options, together with important model options, in Table (2.1) and can be activated/de-activated separately.

Options	Meaning/Inclusion in	Default Setting
1	Roller radiation stresses S^r_{jk} in mom. eq.	On
2	Lateral mixing coefficient with D^r	On
3	Contribution of rollers in stir. velocity u_{stir}	On
Friction dissipation	D^f in wave energy E due to bot. friction	Off
Wind forcing	Wind shear stress τ_{wi} in mom. equation	Off
Friction formulation	Bed shear stress τ_{bi}: Feddersen et al.,(2000)	On
Wave/current interaction	Doppler shift and energy equations	On
Refraction	Global Snell Law	On
Diffraction	Diffraction of waves due to vertical objects	Off
Sediment	Soulsby & van Rijn total load sed. transport	On

Table 2.1: Model options, their meaning and their settings.

2.2 The Morfo62 model

The Morfo62 model (Calvete et al., 2005, Ribas, 2003) is employed as an additional tool in order to test whether the results of Morfo55+ in the initial stages of bar formation are in agreement with linear stability analysis (LSA). A description of the basic theoretical background of Morfo62 is given in this section.

2.2.1 Linear stability analysis

The system of equations that Morfo62 analyzes is the same as the ones presented in Subsections (2.1.3 and (2.1.4). The substantial difference with Morfo55+ is that Morfo62 is based on linear stability analysis. This means that the model investigates the initial evolution of small bed perturbations superimposed on a basic state, in order to yield information about the stability of the latter.

To perform linear stability analysis, first a basic state must be obtained. This is stationary and alongshore uniform; it represents the equilibrium values of the system variables under a steady bottom profile. Under this consideration, small alongshore periodic bed perturbations can be superimposed on this basic state. For the bed level $z_b\left(x,y,t\right)$ this reads

$$z_b\left(x,y,t\right)=z_{b0}\left(x\right)+h\left(x,y,t\right)\ , \tag{2.42}$$

where $z_{b0}\left(x\right)$ represents the basic state for the bed and $h\left(x,y,t\right)$ describes the small perturbation, which is allowed to evolve in time. For the perturbation it follows

$$h_{M62}\left(x,y,t\right)=\Re\left\{h_{M62}\left(x\right)\exp\left[ik_{M62}y+\omega_{M62}t\right]\right\}\ , \tag{2.43}$$

where $k_{M62}=2\pi/\lambda_{M62}$ is the corresponding wavenumber, describing the spatial periodicity of the perturbation in the loghshore direction, λ_{M62} is the related wavelength and ω_{M62} is the complex frequency. For the solution to have a physical meaning, only the real part (denoted by the symbol $\Re$) is taken into account. Expressions like (2.42) and (2.43) are formulated for the rest of the dependent variables of the system.

The expressions (2.42) and (2.43) are inserted into the equations described in Subsections (2.1.3) and (2.1.5). The fact that the perturbations are small compared to the basic state, i.e. $|h_{M62}|\ll|z_{b0}|$, allows for a linearization of the system. This is done by keeping only the terms that depend linearly on the perturbations. This procedure yields an eigenvalue problem: to each small perturbation (2.43) corresponds a number of different eigenvalues ω_n $(\mathrm{n}=1,2,...)$, that rise as the necessary restrictions for the system to obey the imposed solutions. These eigenvalues ω_n characterize the different growing modes n and are complex. Thus it follows

$$\omega_{M62}=\omega_{real}+i\omega_{im}\ , \tag{2.44}$$

The subscript *real* represents the real part of the eigenvalue describing the growth rate of the bed perturbation: it will grow for $\Omega_{M62}=\Re\left(\omega_{M62}\right)>0$ or it will decay for $\mathit{\Omega}_{M62}<0$. In the first case the the basic state is unstable: convergence of sediment transport occurs over the crests of the bed and the perturbations grow. On the other hand, when $\Omega_{M62}<0$ divergence of sediment occurs over the bed and the perturbations get damped: the basic state is stable.

The imaginary part of expression (2.44), denoted with the subscript *im*, represents the phase speed of the perturbation h, i.e.

$$c_{M62}=\frac{-\Im\left(\omega\right)}{k_{M62}}$$

also called the migration rate $c_{M62}=V$ (m day^{-1}). If $V\neq0$, then the bed perturbations migrate in the longshore direction. This happens when divergence of sediment transport occurs upstream of the bar and at the same time convergence of sediment transport occurs downstream. Subsequently, the bar grows downstream and gets eroded upstream, which leads to its migration.

From the perturbations that result in instabilities, eventually one will dominate the dynamics of the system. This is referred to as the fastest growing mode (FGM) and is associated with the highest growth rate $\Omega_{M62m} = \Omega_{FGM}$ and with a corresponding wavenumber $k_{M62m} = 2\pi/\lambda_{M62m}$. The properties of this perturbation can be representative of how bed patterns grow during the initial stage of their formation.

Chapter 3

Methodology

In this chapter the experimental setup, the methods to analyze model results and the description of the model experiments are presented. The use of each of these methods is essential in order to answer the research questions that were formulated in Chapter 1.

Hereafter, three sections follow. First, the setup of the experiment for the default case is provided (Section 3.1). After that, Section (3.2) describes the methodology to analyze the results obtained with Morfo55+, in order to describe the basic state and the initial growth of bars and to compare results with the Morf62 model, which employs linear stability analysis. Finally, quantitative measures of the bar characteristics in the finite amplitude regime are given in Section (3.3), in order to assess the effect of the rollers in long-term evolution of sand bars.

3.1 Design of the experiment; default case

The imposed longshore averaged bottom profile of the domain (Fig. (3.1)) is similar to the one that has been used in the study of Yu & Slinn (2003) and Garnier et al. (2008). It has a sloping bottom towards the shore with a longshore uniform bar crest.

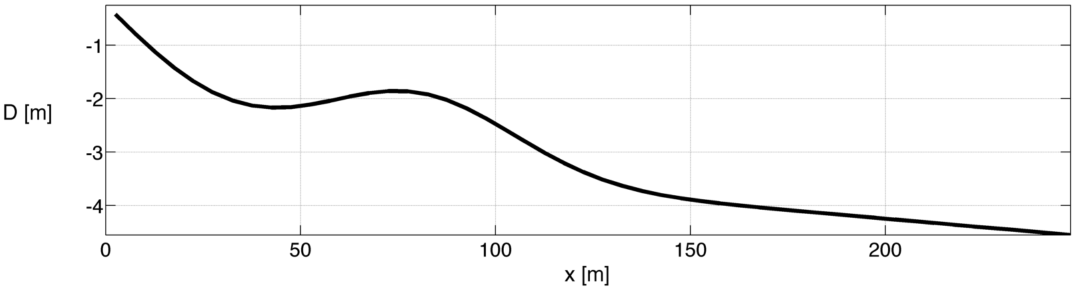

Figure 3.1: Initial bathymetry.

The peak of the crest is located at the cross shore direction at $x = 80$ m away from the shoreline. More details about the bottom profile formulation and the parameters used are given in Appendix A. This setting is representative for a real beach system, like the one in Duck, North Carolina, USA. The length of the domain (longshore direction) L_y is 2000 m and its width (cross-shore direction) L_x is 250 m. The cross-shore direction is chosen so that it comprises the full width of the surf zone under the present wave breaking conditions. The point, at which the bottom is allowed to change defines the time $t = 0$ days for all the simulations. The values at $t = 0$ days are part of the initial conditions of the perturbed system. These profiles are the basic state solutions for the variables with no bottom perturbations h superimposed on the equilibrium bed z_{bo} (Fig. (3.1)).

The waves are assumed to be normally incident to the shore, i.e. $\theta = 0^o$. Their properties are prescribed at the offshore boundary by a root mean square wave height $H_{rms}^{off} = 1.5$ m and a peak period $T_p = 7.5$ sec . These are typical conditions that frequently occur at the Duck site (Konicki & Holman, 2000). Roller dynamics are fully included in the default case. For the default case the numerical parameters, the parameters of the model and the configuration are summarized in Tables (3.1) and (3.2) .

Parameter	Meaning	Default Value
$\triangle x$	cross-shore grid step	5 m
$\triangle y$	longshore grid step	10 m
L_x	width of the domain	250 m
L_y	length of the domain	2000 m
$\triangle t$	hydrodynamical time step	0.05 sec
moac	morphological acceleration factor	20
$\triangle t_{\mathrm{morpho}}$	morphological time step ($\triangle t \cdot \mathrm{moac}$)	1 sec

Table 3.1: Main numerical settings for the default case with Morfo55

Differences in the values of parameters between the default case and similar studies, for example Ribas et al. (2011), concern the apparent bed roughness $k_a = 0.7$ m, the saturation ratio $\gamma = 0.6$ and the root mean square wave height $H_{rms} = 1.5$ m (values of that article $k_a = 0.035\,\mathrm{m}$, $\gamma = 0.475$ and $H_{rms} = 1$ m). The values of the parameters in this study are within the range that is commonly used (see for example Table 1 in Ribas et al., 2011) so that the corresponding conditions resemble the ones of natural beach systems. Finally, the value of the bedslope coefficient is $\gamma = 5$, following Garnier et al. (2008).

Hydrodynamics

Parameter	Physical Meaning	Default Value
g	Acceleration due to gravity	$9.81\ \mathrm{ms}^{-2}$
γ_b	Index of wave saturation	0.6
B	Breaker coefficient	1
c_D	Bottom friction drag coefficient	$0.5 \cdot 10^{-2}$
k_a	Apparent bed roughness	$7 \cdot 10^{-2}$ m
M	Turbulence dissipation parameter	1
β_{rol}	Slope of wave/roller front	0.05
θ^{off}	Offshore wave angle of incidence	0^o
H_{rms}^{off}	Offshore rms wave height	1.5 m
T_p	Peak wave period	7.5 sec

Morphodynamics

Parameter	Physical Meaning	Default Value
p	Porosity of the bed	0.4
d_{50}	Median grain size of sediment	$0.2 \cdot 10^{-3}$ m
γ	Donwslope sediment coefficient	5
n_{bor}	Rollers parameter for stirring velocity	50

Table 3.2: Summary of parameters, their meaning and their values for the default case. Top: settings for the hydrodynamics. Bottom: settings for the morphodynamics.

3.2 Basic state and initial formation of bars

The first part of the study focuses on the investigation of the cross-shore profiles of the variables in the basic state and the description of the spatial and temporal characteristics of the initially growing bed patterns. This will be done by considering and comparing two cases, i.e. the default configuration (Section 3.1) and a roller-off configuration, in which $S_{ij}^r = 0$, $D^r = D^w$, $n_{bor} = 0$ in equations (2.18), (2.21) and (2.31), respectively.

3.2.1 Methods to analyze results with Morfo55+

To check the Morfo55+ model for the consistency of its results, the growth rates and the growth times of the emerging bed patterns for their initial growth are needed. There are two ways of computing these properties that are used here: first, by analyzing the evolution in time of the Fourier transform of the bed perturbation $h\left(x,y,t\right)$ and second, by analyzing the evolution of the bed perturbation $||h||$ and the global growth rate σ.

3.2.1.1 Growth rates from Fourier analysis

The first method to retrieve the growth rate of small bed forms is by considering the alongshore uniform bed profile $z_b\left(x,y,t\right) = -z_{b0}\left(x\right) + h\left(x,y,t\right)$ of Section (3.1) and by writing the corresponding bed perturbation $h\left(x,y,t\right)$ as a Fourier series of the form:

$$h\left(x,y_j,t\right)=\sum_{n=1}^{N}H\left(k_n,x,t\right)\exp\left[ik_ny_j\right]\ , \tag{3.1}$$

where $H\left(k_n,x,t\right)$ is the amplitude of the perturbation, with $y_j=j\triangle y$ with $j=1,2..N_y$ and wavenumber k_n in the longshore direction

$$k_n=\frac{2\pi\left(n-1\right)}{L_y},\ \ n=1,2...N\ , \tag{3.2}$$

By inverting (3.1) and choosing a fixed location $x=x_o$ the amplitude H follows

$$H\left(k_n,x_0,t\right)=\sum_{j=1}^{N_y}h\left(x_0,y_j,t\right)\exp\left(-ik_ny_j\right)\ . \tag{3.3}$$

At the initial stage of the simulations with Morfo55+ the perturbations are expected to behave according to linear stability theory, i.e. allowing to approximate the amplitude $H\left(k_n,x_0,t\right)$ as,

$$H\left(k_n,x_0,t\right)\approx H\left(k_n,x_0,0\right)\exp\left[\omega_nt\right]\ , \tag{3.4}$$

with ω_n being the frequency and the initial amplitude of H. By taking the logarithm of the modulus of expression (3.4),

$$\ln\left(\left|H\left(k_n,x_0,t\right)\right|\right)\approx\Re\left(\omega_n\right)t+\ln\left(\left|H\left(k_n,x_0,0\right)\right|\right)\ . \tag{3.5}$$

The growth rate $\Omega=\Re\left(\omega_n\right)$ is the slope of (3.5), which describes a straight line. For the dominant Fourier mode the growth rate is $\Omega_m=\max\left\{\Re\left(\omega_n\right)\right\}$. Subsequently, the wavenumber for $k_n\to k_m$ is $\lambda_m=2\pi/k_m$.

3.2.1.2 Growth rates from global variables

An alternative way of obtaining information about the initial formation of bars with the Morfo55+ model is by using the global growth rate. First, the averaging over the whole domain for a variable f of the system is defined. It reads

$$\overline{f}=\frac{1}{L_yL_x}\int_0^{L_y}\int_0^{L_x}f\ dxdy\ , \tag{3.6}$$

The global growth rate is defined as (Garnier et al., 2006)

$$\sigma\equiv\frac{1}{||h||^2}\frac{\partial}{\partial t}\left(\frac{1}{2}||h||^2\right)\ , \tag{3.7}$$

with $||h||^2$ being the spatial variance of the bedforms, given by

$$||h||^2=\left(\overline{h^2}\right)\ , \tag{3.8}$$

For small amplitude bars, $||h||=\left(\overline{h^2}\right)^{1/2}$ can be expressed in the same way as in (3.4), i.e $||h|| \approx ||h_o|| \exp{[\sigma t]}$, where $||h_0||$ is the initial value of $||h||$, so that its logarithm yields

$$\ln{(||h||)} \approx \sigma t + \ln{(||h_0||)} \ , \tag{3.9}$$

with $||h_0||$ being the initial value of the amplitude $||h||$. In the linear regime, expression (3.7) or (3.9) should be identical and yield growth rates that are in accordance with those obtained from linear stability theory.

3.2.1.3 Identifying the limits of the linear regime

For the most part, this study aims to present and then analyze a sand bar state where the growing of the bed perturbations is not infinitesimal compared to the initial topography. The evolution of the global growth rate is analyzed in order to identify when the linear regime of the bar formation ends. To illustrate this, a conceptual picture of the global growth rate σ as a function of time is shown in Fig.(3.2). At the beginning of the bar evolution, a selection between various modes occurs, which is depicted in the figure as an increase of σ in time. After some time, the dynamics of the system are controlled by the perturbation with the fastest growing mode and therefore σ is constant in time. This is the linear regime of bar formation, defined by the two vertical dashed lines in Fig.(3.2). In this regime, the amplitude A_m of the bars grows exponentially in time (not shown). Due to the nonlinear character of the system, the interaction of different modes becomes evident after a certain period of time. This is shown in this figure with a change of the growth rate σ, which is no longer constant (regime bounded to the left by the second vertical line in Fig.(3.2)) . The change in σ is used here to define the onset of the nonlinear interactions in the system, something that will be referred to as the finite amplitude regime of the bed formations. A nonlinear model, such as Morfo55+, in principle could give rise to all kinds of possible sand bar states (further growing of bars, saturated state and negligible growth rate, periodic growth rate, chaotic behavior, etc) for longer times of beach evolution.

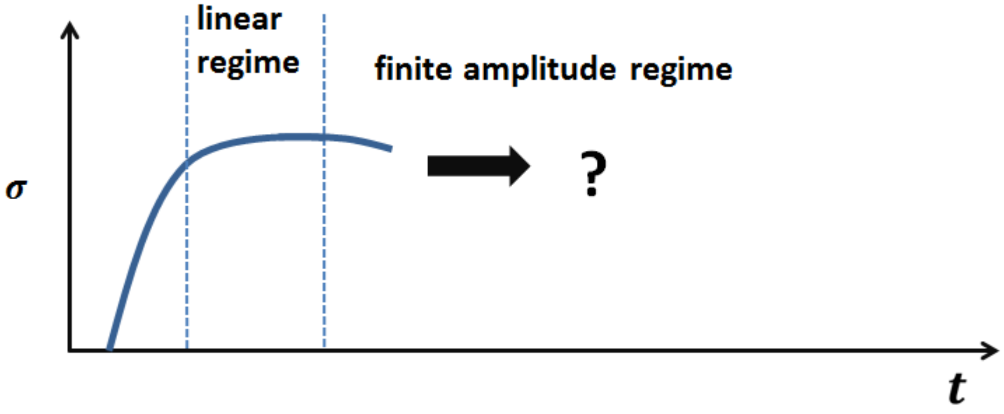

Figure 3.2: Conceptual picture of the different stages of the growing of bars in the surf zone. The evolution of the global growth rate σ in time t is analyzed to distinguish the different regimes. The linear regime and the finite amplitude regime are highlighted.

3.3 Effect of rollers on the bar characteristics in the finite amplitude regime

In order to quantify the effect of the surface rollers in the long-term evolution on the growing bars several parameters are defined which describe their characteristics like the amplitude, the wavelength and the growth rate.

3.3.1 Parameters describing the bar properties

There are two types of parameters that characterize the bars either spatially or temporally. The spatial characteristics are measured by four parameters:

- ▷ The amplitude of the bars $A_m = \frac{1}{2}\left(\max\left(h\right) - \min\left(h\right)\right)$, given in meters (m), where the maximum and the minimum values of the perturbations h of the whole physical domain are taken into account.
- ▷ The global bed perturbation amplitude, also called the root mean square amplitude, $||h||$ given by the square root of Eq.(3.8) in meters (m).
- ▷ The mean wavelength $\lambda_{mean} = L_y/N_{bar}$ of the bars, also referred to as the mean spacing of the bars. It is the ratio of the longshore distance of the beach L_y and the number of the emerging bars $N_{bar}$and it describes the distance at the longshore direction between two consecutive crests of the bed.
- ▷ The dominant wavelength $\lambda_m = \lambda_{max}$ of the bars. It is defined from Fourier analysis (subsection 3.1.1) and gives the spacing between two consecutive bar crests for the dominant Fourier mode.

The temporal behaviour of the bars is characterized by two following parameters:

- ▷ The growth rate of the dominant Fourier mode $\Omega_m = \max\left\{\Re\left(\omega_n\right)\right\}$, described in subsubsection (3.2.1.1),
- ▷ The global growth rate σ defined by expression (3.7).

Chapter 4

Results: basic state and initial formation of bars

In this chapter the basic state and the initial formation of the bars are presented. This chapter will yield answers on the first two research questions of the introduction. It is aimed to a) show and to compare profiles of variables at the initial state between the default case and the case without rollers (first research question) and b) describe the initial formation of bars and to quantifying the extent by which the nonlinear model Morfo55+ is able to reproduce their characteristics, as obtained with the Morfo62 model, which employs LSA (second research question).

4.1 Basic state

Two different cases are presented in this section: the default case with the parameter values and the settings as described in Section (3.1) and the roller-off case, in which $S^r_{ij} = 0$, $D^r = D^w$, $n_{bor} = 0$ in equations (2.18), (2.21) and (2.31), respectively.

First, Morfo55+ is spun up. It turns out that the values of the variables reach an equilibrium under a steady bottom profile in approximately 50 mins (not shown). In Fig.(4.1a) the profiles of the wave energy E^{w0} for the two cases are plotted versus the cross-shore distance x. For both cases E^{w0} is decreasing towards the coast starting from 2.7 kJm^{-2} at the offshore boundary to 0 kJm^{-2} at the shoreline (x = 0 m). The most significant decrease in E^{w0} occurs over the longshore bar ($x = 80\,\mathrm{m}$) and the inner surf zone ($x <$ 20 m). This is where most of the wave breaking occurs. In general the two profiles are similar, with the roller-off case (red dashed line) being slightly larger than the default case. The largest difference between the two is seen in the inner surf zone ($x <$ 20 m).

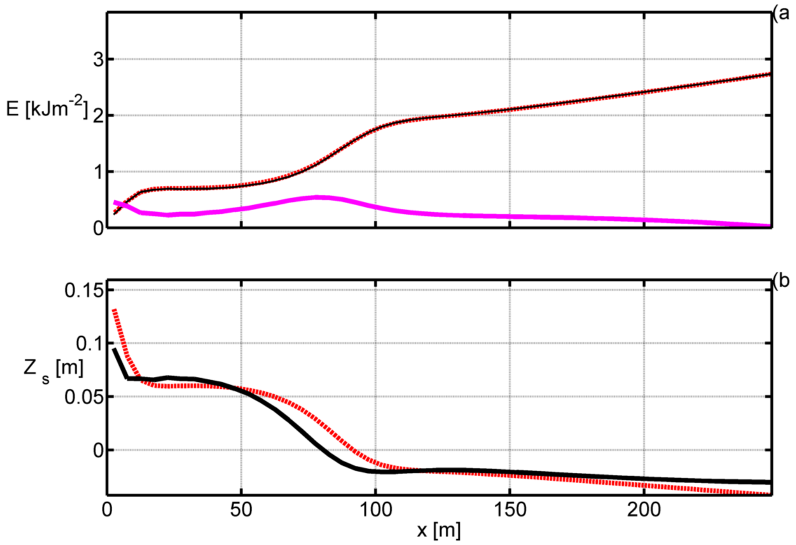

Figure 4.1: a) wave energy E^{w0} and roller energy E^{r0} (purple line) versus cross-shore distance x of the basic state and b) As in a, but for the sea level z_s^o. The notation o denotes the value of the variable for the basic state. Black colour indicates the values for the default case and red color indicates values for the roller-off case.

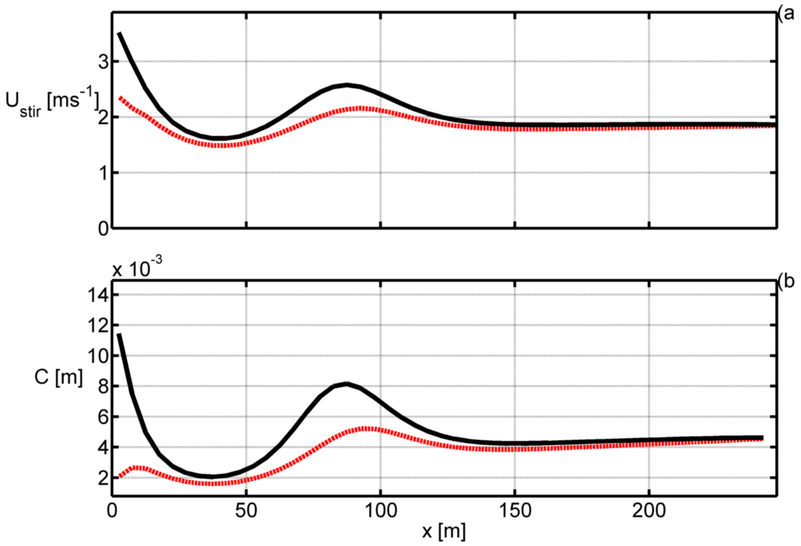

Figure 4.2: As Fig.(4.1), but a) stirring velocity u_{stir}^o versus cross-shore distance x of the basic state b) integrated volumetric sediment concentration C^o.

The purple line in the same figure describes the profile of the roller energy E^{r0} of the basic state for the default case. The profile of E^{r0} is clearly different than E^{w0}. For the most part, the roller energy increases where the wave energy decreases. This implies that the energy that is dissipated from wave breaking feeds the roller energy (see eq. (2.10) and eq. (2.12)). The difference in the behaviour between the two (black and purple line in Fig.(4.1b) is more pronounced above the longshore bar and very close to the shoreline. In between the two locations both the wave energy and the roller energy slowly decrease.

The profiles of the mean sea level z_s^0 are shown in Fig.(4.1b) for the default and the roller-off case. Again, the changes are distinguishable where the longshore bar is located and the inner surf zone. The set-up of the mean sea level, caused by the breaking waves and the changes in the amplitude of the crests and troughs, is larger for the roller-off case (red line) above the longshore bar and close to the shore.

Profiles of basic state variables associated with sediment transport are plotted in Fig.(4.2). Starting from the top panel, the influence of the rollers in increasing the stirring velocity u_{stir}^0 and thus the bed shear stress in Fig.(4.2a). In particular, the resuspension of sediment due to the roller turbulent bores (eq. (2.24)) in u_{stir}^0 is evident in the maxima of the default case profile (black line), which are larger than the roller-off case. This difference is also depicted in the other two panels of this figure, with the maxima being larger for the default case in both sediment concentration C^0. The value of the concentration is almost ten times larger (Fig.4.2b) between the default and the roller-off case. In fact, it is interesting that C^0 exhibits a second peak at the shoreline for the default case (the first one is located at $x = 80$ m), whereas the peak is shifted shorewards for the red curve of the roller-off case.

4.2 Characteristics of initially growing sand bars

4.2.0.1 Growth rate from global analysis

The method described in Chapter 3 is followed and the evolution of the global bed perturbation $||h||$ is analyzed. The global growth rate σ (d^{-1}) and $||h||$ (m) are computed by using expressions (3.7) and (3.8), respectively. The profiles of these quantities are plotted versus time for the default case in Fig.(4.3) (σ, $||h||$ at the top and middle panels, respectively).

The slope of $\ln(||h||)$ gives the growth rate $\Omega_{||h||} = 0.072\ \mathrm{h}^{-1}$ and the growth time $t = 1/\Omega_{||h||} = 14$ h. The subscript $||h||$ denotes the method that the growth rate is derived with. The behaviour of σ versus time (top panel in the Fig.(4.3)) is followed in order to determine where the initial formation of bars ends. Until $t \sim 1.5$ days σ increases in time, implying that a selection of the different modes occurs.

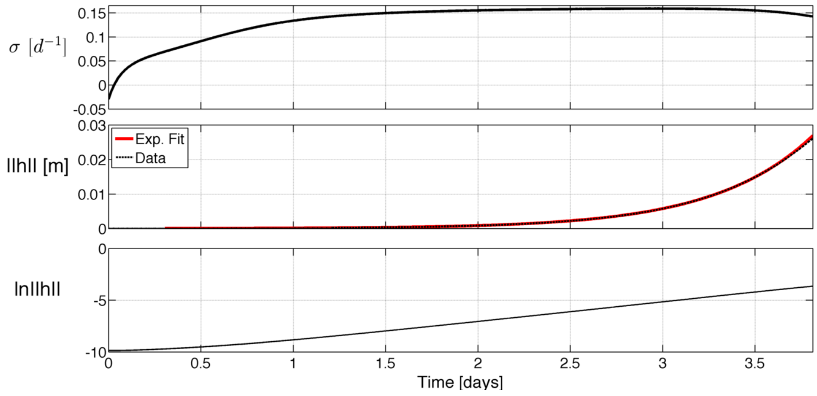

Figure 4.3: Top panel: Global growth rate σ (d^{-1}). Middle panel: Global perturbation $||h||$ (m). Bottom panel: logarithm of $||h||$ when $||h||$ is assumed to follow LSA in the linear regime. The results are for the default case

After that point, the global growth rate has a constant value, $\sigma = 0.15$ d^{-1}, between 1.5 and 2.4 days, which is the regime where the pattern formation is dominated by the fastest growing mode, also called the linear regime. Finally, a change in σ is observed at $t \simeq 2.4$ days, as its value starts to decrease.

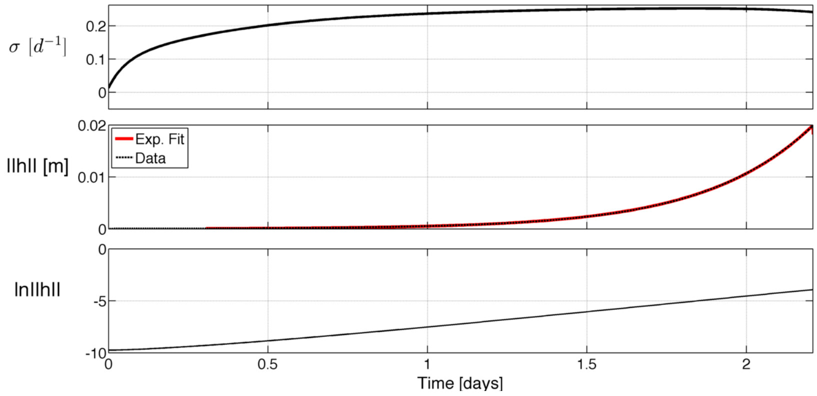

Figure 4.4: As in Fig.(4.3), but for the roller-off case.

For the roller-off case, sand-bar formation occurs faster, something that is clear from Fig.(4.4). Again, the bar amplitude (middle panel in this figure) grows exponentially until $t \simeq 2$ days. This is the linear regime for the roller-off case. The slope of its logarithm (bottom panel) gives $\mathit{\Omega}_{||h||} = 0.11$ h^{-1} or $t = 9.5$ h. Following the behaviour of σ in time (top panel), two things are highlighted: first, that the bar system forms faster (larger growth rate) than it does in the default case and second, that the changes in bar growth occur in a shorter time period compared to the former case.

4.2.0.2 Spatial and temporal characteristics

The perturbations h are plotted in plan view for the default case (Fig.4.5) after $t = 1.4$ days (top) and $t = 2$ days. The flow associated with these patterns is also shown in the figure (by vectors). Rip channel systems are present mostly shoreward of the longshore bar ($L_x \simeq 60$ m). In both panels of Fig.(4.5), the patterns are more pronounced between $L_y = 400 - 800$ m. Bars also form close to the shoreline, $L_x = 20$ m and they are out of phase with the bars at $L_x \simeq 70$ m. The amplitude the patterns is in the order of $\sim 10^{-2}$ m after 2 days (bottom panel). Jet-like flow is moving offshore in the channels and shoreward over the shoals, resulting in a cell-like circulation. Here, the wavelength λ_{mean} of the rhythmic features is determined at $L_x \simeq 60$ m, by dividing the length of the domain $L_y = 2000$ m and the number of bars N_{bar}(see also Subsection 3.3). For $t = 1.4$ days, top panel, $\lambda_{mean} = 285$ m ($\mathrm{k_{mean}} = 0.022$ m^{-1}) and at $t = 2$ days (bottom panel) $\lambda_{mean} = 250$ m ($\mathrm{k}_{mean} = 0.025$ m^{-1}).

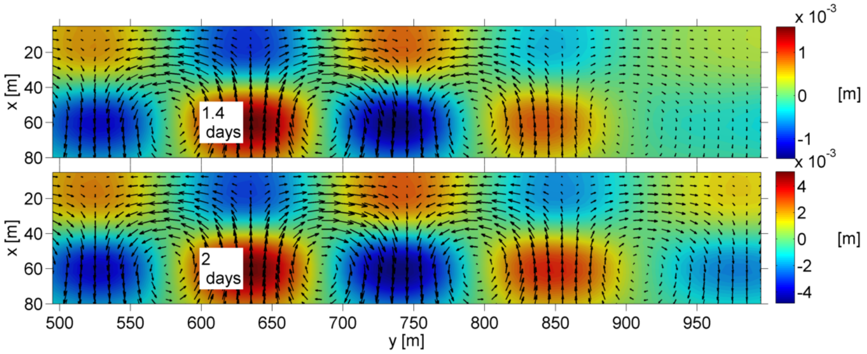

Figure 4.5: Plan view of bottom perturbations h for the default case, obtained with Morfo55+. Top: h after $t = 1.4$ days. Bottom: h after 2 days. Crests are in red color and troughs are in blue color. The vectors represent the currents.

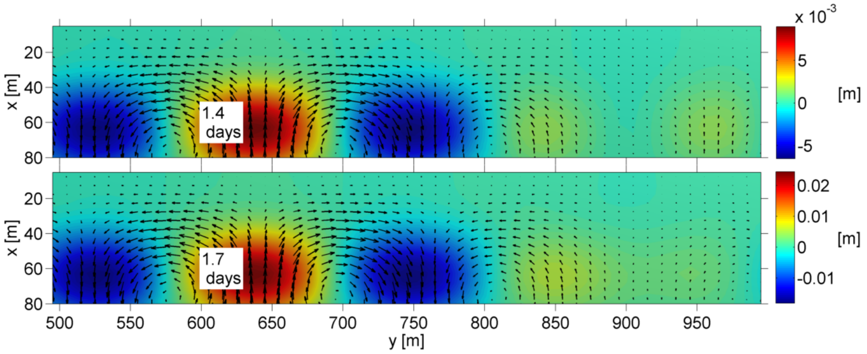

Figure 4.6: As in Fig.(4.5), but for the roller-off case.

For the roller-off case the spatial patterns of the perturbations h and the currents $\mathbf{v}$ are plotted in Fig.(4.6). Again, bars form in the domain and the associated flow behaves the same way as in the default case (offshore currents in the channels, onshore currents over the shoals). The bars emerge simultaneously over the entire domain. The bottom patterns reach an amplitude of ~ 0.02 m in $t = 1.7$ days. In this case, the main bar line is located at $x \sim 60$ m, but there is not separate crest-trouph-crest sequence forming at the shoreline. The wavelength is $\lambda_{mean} = 285$ m after $t = 1.7$ days ($\mathrm{k}_{mean} = 0.022\ \mathrm{m}^{-1}$).

To quantify the differences in the hydrodynamics between the two runs, the perturbed mean sea level $z_{sper} = z_s - z_s^0$ and the wave energy $E^w_{per} = E^w - E^{w0}$ are plotted in Fig.(4.7). Again, the circulation pattern is superimposed over z_s in the left panels of the figure. Results are shown for a plan view of a part of the domain after $t = 2$ days and $t = 1.7$ days of morphological evolution for the default case (top) and roller-off case (bottom), respectively. At this stage, $z_s^{'}$ is smaller when rollers are added to the system (top left panel), than without the rollers, i.e. $S^r_{ij} = 0$, $D^r = D^w$, $n_{bor} = 0$. However, it is shown that there is set-up and set-down close to the shoreline for the default case (top left panel). For both cases, the rest of the pattern is similar. For the perturbed wave energy E^w_{per} (right panels) the pattern is more clear. When rollers are activated (top right panel) there are alongshore periodic patterns of E^w_{per} at $x \sim 70$ m and in the inner surf zone. These are out of phase with each other. This is not the case where rollers are de-activated (bottom right panel): E^w_{per} is again alongshore periodic in the surf-zone ($x = 20 - 70$ m), but there is not an out of phase separate pattern very close to the shoreline. Note that, values of E^w_{per} are almost 10 times smaller for the default case compared to the roller-off case.

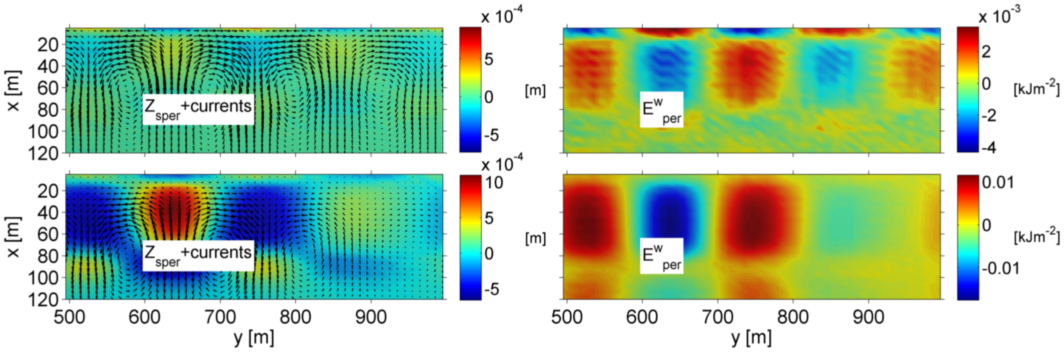

Figure 4.7: Left panels: Plan view of the current circulation $\mathbf{v}$ superimposed on contours of perturbed mean sea level z_{sper} after $t = 2$ days. Top: default case. Bottom: roler-off case. Right panels: Contour plot of the perturbed wave energy E^w_{per} after $t = 1.7$ days. Top: default case. Bottom: roller-off case.

A comparison of the patterns of the E^w_{per} with the those of the perturbed roller energy E^r_{per} (Fig.(4.8)) is feasible. Interestnigly, where there are negatives (positive) values of E^r_{per} near the shoreline, the perturbed wave energy E^w_{per} is positive (negative). This is also the case across the longshore bar, where most the wave breaking occurs (and energy is dissipated).

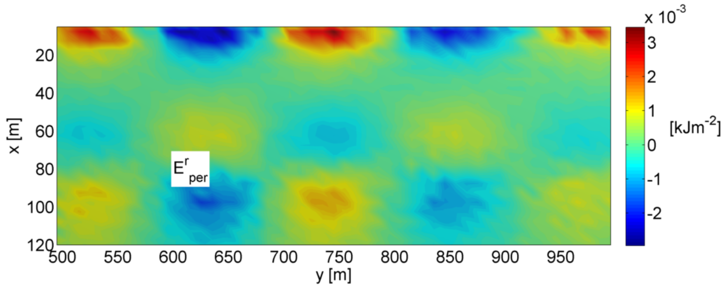

Figure 4.8: Perturbed roller energy E^r_{per} after $t = 2$ days for the default case.

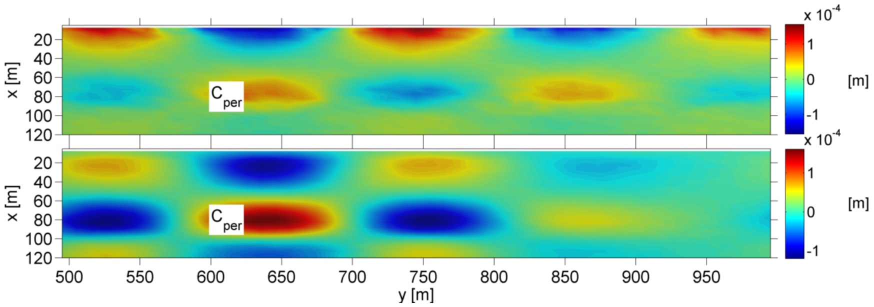

Figure 4.9: Plan view of the perturbed depth integrated concentration C after $t = 2$ days and $t = 1.7$ days of evolution for the default case (top) and the roller-off case (bottom), respectively.

Fig.(4.9) shows contours of the perturbed integrated sediment concentration C_{per} at $t = 2$ days and $t = 1.7$ days for the default case (top) and roller-off case (bottom), respectively. Values between the two cases are similar, but the distribution is different. The largest concentration values are located very close to the shore for the default case (top panel of Fig.(4.9), whereas the maxima for the roller-off configuration (bottom panel of the same figure) are located at $x = 80$ m, slightly offshore of the longshore bar. For the former case, there is also a pattern over the longshore bar, but it located shoreward approximately at $x \sim 90$ m with smaller values, compared to the roller-off case.

4.2.0.3 Fourier analysis

Methods in order to obtain wavenumbers and wavelengths, as well as growth rates and e-folding times with Morfo55+ are used, following the subsequent methodology that was described in Section (3.2). Here, a Fourier decomposition of the amplitudes of the bed perturbations h is performed. The most representative mode that dominates the dynamics of the perturbations at x_o at the initial stage of formation is the dominant Fourier mode. The cross-shore location at $x_o = 52.5$ m is chosen shorewards of the longshore bar. The evolution in time of the amplitude $H\left(k_m, x_0, t\right)|$ of the bottom perturbation $h(x_0, y, t)$ (given by expression (3.3)) is shown in Fig. (4.10) for the default case. This result allows for expression (3.3) to be written as (3.4). Subsequently, the logarithm of the modulus of (3.4) for $|H\left(k_m, x_0, t\right)|$ is described by a straight line (given by (3.5)). The latter is plotted as a function of time in Fig. (4.11).

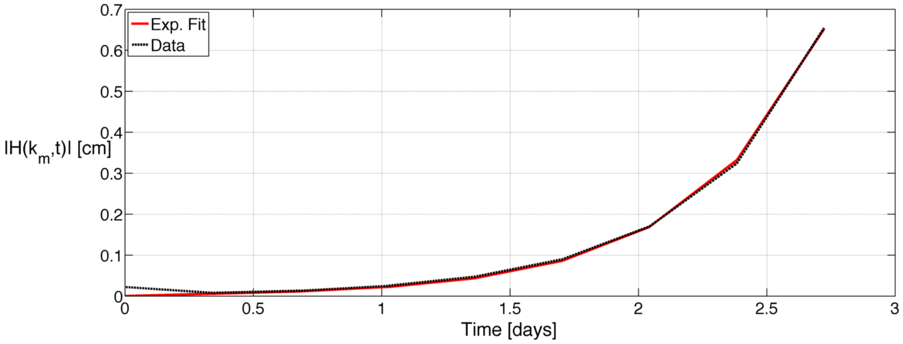

Figure 4.10: Black dashed line: evolution of dominant Fourier mode $H\left(k_m, x_0, t\right)||$ for $k_n \rightarrow k_m$ for Fourier transformation of $h\left(x_0, y, t\right)$ at $x_o = 52.5$ m. Red line: the corresponding exponential fit to the data. Results are for the default case.

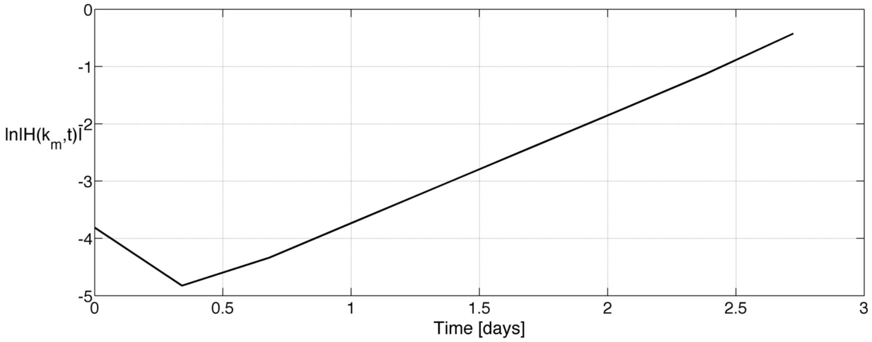

Figure 4.11: Logarithm of the modulus of the dominant Fourier mode $|H\left(k_m, t\right)|$, Fig.(4.10), given by expression (3.5) for the default case.

The slope of (3.5) (Fig.4.11) provides the growth rate $\Omega_m(\mathrm{d}^{-1})$. The result is $\mathit{\Omega}_m = 0.078\ \mathrm{h}^{-1}$ with a growth time $t_m = 1/\Omega_m = 13$ h. The associated wavelength λ_m of the dominant mode is retrieved from the model output and plotted in Fig.(4.12). The transitions between different wavelengths λ_m have been omitted (increase in λ_m values in the beginning of the simulation).

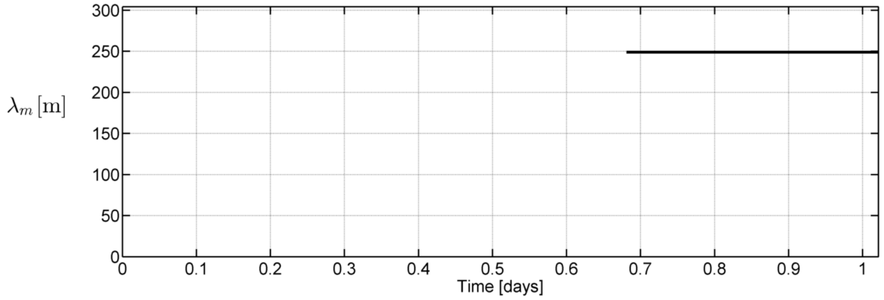

Figure 4.12: Dominant wavelength λ_m as a function of time, according to Fourier analysis for the default case.

The wavelength is $\lambda_m = 250$ m between $t = 0.7 - 1.5$ days, i.e. $k = 0.021$ m^{-1} From Fig.(4.12) it is evident that for t $<$ 0.7 days the spacing of the bed patterns at x_o keeps on changing; it is increasing until $\lambda_m = 250$ m ($t = 0.7$ days). Fourier analysis is also used for the roller-off case. Here, only the plot of the logarithm of $|H\left(k_m, t\right)|$ is shown (Fig.(4.13), which shows again a straight line, implying that the amplitude of the dominant Fourier mode grows exponentially in time. The growth rate is $\Omega = 0.12$ h^{-1}and the e-folding time $t_m = 8.3$ h. The corresponding wavelength for $k_n \to k_m$ is $\lambda_m = 250$ m and after $t = 0.7$ days it does not change anymore (not shown).

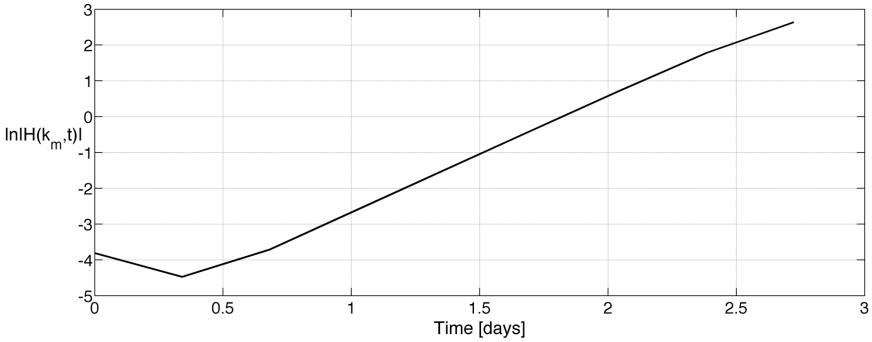

Figure 4.13: As Fig.(4.11), but for the roller-off case.

4.2.0.4 Morfo62 results

Morfo62 is run with similar settings for the default case for a range of wavenumbers $k_{M62} = 0.010 - 0.060$ m^{-1}. This way bars of different wavelengths are able to form in the domain. The growth rates Ω_{M62} with Morfo62 are plotted as a function of wavenumber k_{M62} in Fig.(4.14) for the default configuration.

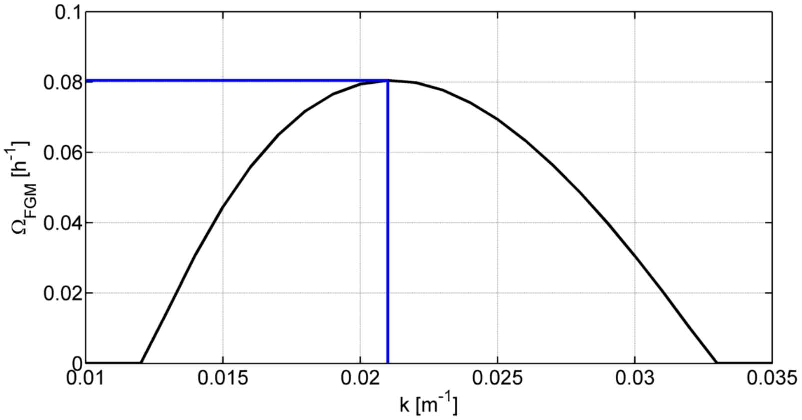

Figure 4.14: Growth rate, Ω (h^{-1}), as a function of wavenumber, k (m^{-1}), computed with Morfo62 for the default configuration. Blue line indicates the fastest growing mode growth rate and wavenumber, Ω_{FGM} and k_{FGM}, respectively.

The growth rate and the wavenumber for the fastest growing mode, Ω_{FGM} and k_{FGM}, respectively, are indicated by the blue lines. They read: $\varOmega_{FGM} = 0.081\,\mathrm{h}^{-1}$ for $\mathrm{k}_{FGM} = 0.021$ m^{-1} which corresponds to a wavelength of $\lambda_{FGM} = 299$ m. The growth time for the FGM is $t_{FGM} = 1/\varOmega_{FGM} = 12.4$ h. For $\mathrm{k_{M62m}} > 0.035$ m^{-1}(excluded from Fig.(4.14)) the growth rates are $\mathcal{O}\left(10^{-8}\right)$ h^{-1}. For $L_y = 2000\ m$, the only modes allowed are $\mathrm{k_n} = (2\pi/\mathrm{L_y})\mathrm{n}$ with n being an integer. This yields values of $\mathrm{k} = ..0.0188,\ 0.22,\ 0.0251, ...$ Accroding to Fourier analysis, it was found that $k_m = 0.021$ m$^{-‘}$, which is the closest value to the fastest growing mode, obtained from Morfo62. Subsequently the e-folding time is $t = 13$ h. For the latter, the discrepancy between the results obtained from Morfo62 and Morfo55+ is almost 5%. The analysis of the growth rate from global properties yielded a growth rate $\varOmega_{||h||} = 0.072$ h^{-1} and a growth time $t = 1/\varOmega_{||h||} = 14$ h, which are also close to the results of Morfo62 (almost 15% difference in $e-$folding times).

For the roller case, an equivalent run with Morfo62 and the same analysis of the growth rate versus the wavenumber gives $\varOmega_{FGM} = 0.075$ h^{-1}for $\mathrm{k}_{FGM} = 0.021$m^{-1} (Fig(4.15)). The e-folding time is $t_{FGM} = 13.3$ h. The difference is almost 50% between this result and the growth rate retrieved from the Fourier analysis of the Morfo55+ output ($t_m = 8.3$ h). The analysis of global properties gave $\Omega_{||h||} = 0.11$ and $t_{||h||} = 9.1$ h.

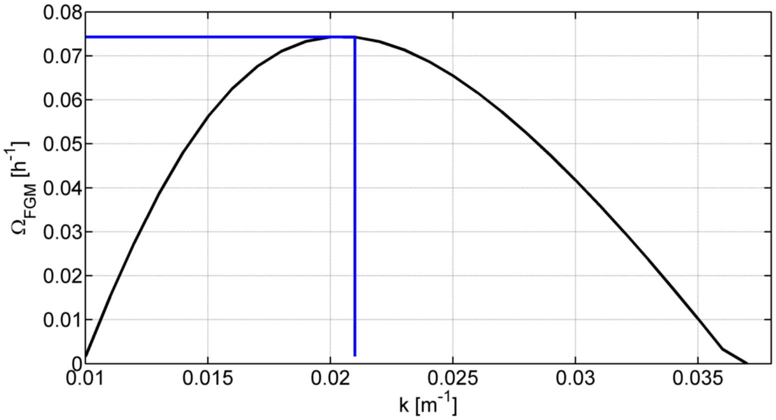

Figure 4.15: As in Fig.(4.14), but for the roller-off case.

Chapter 5

Results: finite amplitude regime of bar formation

5.1 Amplitude, growth, position and flow

Results are presented of the spatial and temporal characteristics of surf zone bars in the finite amplitude regime. In order to address research question 3 of the introduction this is done in both the presence of rollers (default case) and in the absence of rollers ($S^r_{ij} = 0$, $D^r = D^w$, $n_{bor=0}$ in equations (2.18), (2.21) and (2.31) respectively). The final state of the bed profile at $t =$ 15.7 days and the evolution of the maximum bar amplitude A_m (Section 3.3) for the default case is shown in Fig.(5.1)

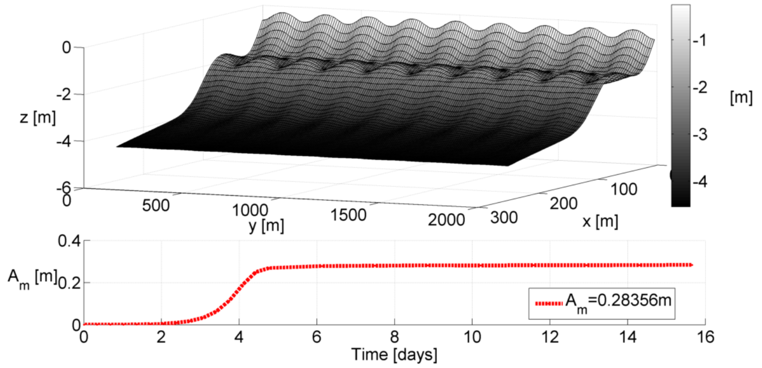

Figure 5.1: Top: final state of the bathymetry of the domain after $t = 15.7$ days. Bottom: evolution of the bar amplitude A_m in tme. Legend indicates the value of A_m at the end of the simulation. Results are for the default case with Morfo55+.

Overall, for $t = 0$ to 15.7 days additional rhythmic patterns that are located mostly between $x = 0 - 120\ m$ have developed over the initial alongshore bar, at $x = 80$ m, . The amplitude of the growing bars is increases from $A_m = 0.001$ m at $t = 0$ days to $A_m = 0.27$ m at $t = 4.5$ days. For the rest of the simulation the amplitude increase is notably smaller: from $t = 5$ to 15.7 days A_m grows approximately 0.01 m, from 0.27 to 0.28 m.

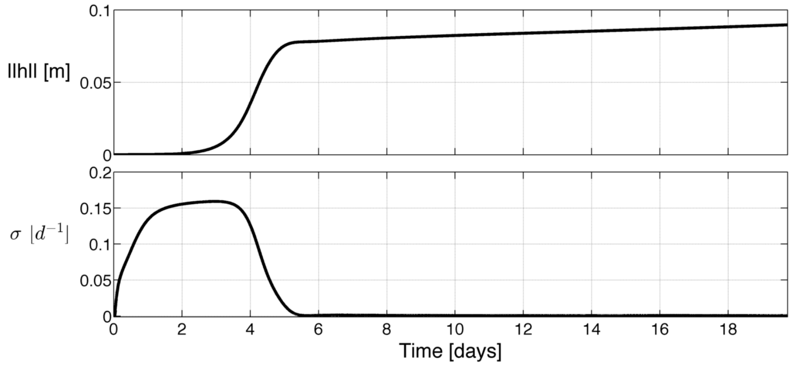

Figure 5.2: Global properties of growing bars. Top: root mean square amplitude of the perturbation $||h||$ versus time. Bottom: global growth rate σ versus time. Resutls are for the default case.

The fact that sand bars grow slowly compared to the first 5 days is highlighted by analyzing the global properties in Fig.(5.2). The evolution of $||h||$ (top panel) and σ (bottom panel) in time are shown. The decrease in σ reveals the nonlinear character of the system and therefore implying that linear stability theory is no longer applicable in order to describe the stability of the bed any further. Interestingly, the global growth rate not only decreases, but also goes to zero after $t \simeq 5.5$ days, having a negligible value (less than 10^{-3} d^{-1}) for the rest of the simulation. This implies that the bars first go through a saturation process and then they reach a so-called saturated bar state, a state in which bars hardly evolve. This criterion for the saturated state, i.e. a bar state characterized by $\sigma \simeq 0$, is given in the past study of Garnier et al. (2008). In spite that the bar amplitude never ceases to increase completely as it is clear for the top panel of Fig.(5.2) and the bottom panel of Fig.(5.1). Nevertheless, this increase is very small.

Another way of investigating the spacing between the bed formations and the limits of the linear regime is with Fourier analysis. The method has been described in subsubsection (3.2.1.1) and the Fourier coefficients $H(k_n, x_0, t)$ ($x_0 = 52.5$ m), given by expression (3.3), are used. For the default case, the normalized modulus of H, with corresponding wavelength λ_n is plotted in Fig.(5.3) (top). Bright colours indicate the dominant modes.

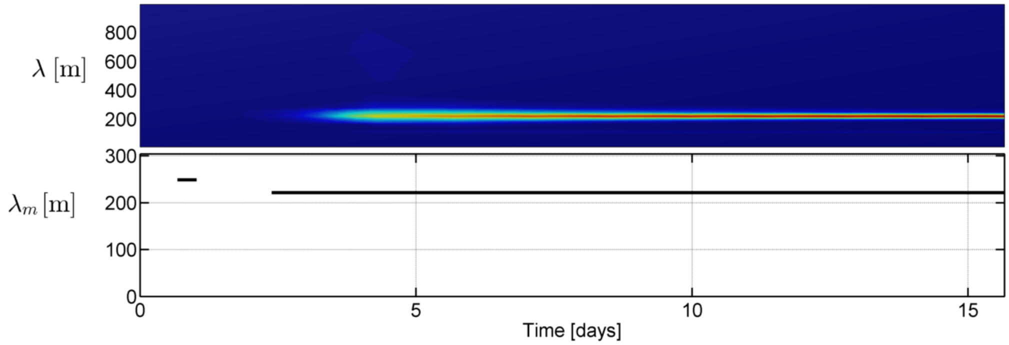

Figure 5.3: Top: Wavelength λ corresponding to the Fourier modes as a function of time. Contours show the normalized modulus of the Fourier transformation $H\left(\lambda, x = 52.5 \text{ m}, t\right)$. Brighter colours indicate the most dominant wavelengths. Bottom: time series of the dominant wavelength λ_m of the Fourier analysis.

According to this figure, several modes interact mostly during the saturation process, i.e. at $t \simeq 4 - 7$ days approximately. The wavelengths of these modes range from $\lambda_n = 180 - 250$ m at $t = 4$ days. After 8 days the wavelength focuses around $\lambda_n = 200 - 220$ m. The bottom panel of Fig.(5.3) is an extension of Fig.(4.12) for the entire beach evolution. The dominant wavelength λ_m jumps from 250 m to 222 m and then remains constant until the final state. Jumps in the wavelength and the decrease of σ indicate that nonlinear effects become evident.

The changes of the bottom patterns between $t = 4.1 - 15.7$ days and their position in the domain are analyzed through Fig.(5.4). The circulation pattern has been added on this figure, indicated by the vectors, in order to relate the currents with the forming sand bars. Crests are indicated by the red colour and troughs by the blue colour.

Bottom patterns consist of alternating bars, over which currents are landward and rip channels, in which seaward currents occur. Channels that are typically narrower than shoals. These resemble crescentic bars, formations that resemble crescentic moons, which are more pronounced at $x \simeq 60$ m and extent along the whole beach, but they are also evident at the shoreline. In general, three main lines of alongshore periodic sand bars are observed in this figure in the cross-shore direction. The first crest-trough-crest sequence is centered at $x \simeq 10$ m, the second line at $x \simeq 60$ m and the third line at $x \simeq 120$ m. The latter is the least pronounced one. Crests are in anti-phase with the channels shoreward. This means that a (trouph) crest offshore is followed by a (crest) trough inshore.

From Fig.(5.4), a change in the bar amplitude is mostly visible between the first two panels on the left (top: $t = 4.1$ days, bottom: $t = 10.2$ days). In fact, bars still grow between that time. Note that, the colorbars are calibrated to show the same range for all the plots. According to Fig.(5.1) the amplitude does not change significantly after $t \simeq 6$ days. In Fig.(5.4), though, between 4.1 and 10.2 days bars grow bigger. This is better seen in Fig.(5.2). Generally, the troughs appear to have smaller amplitudes than the crests do. During the rest of the simulation, differences in the amplitude, the shape or the position of the patterns are more difficult to detect.

Regarding the flow, a rip current circulation is formed, with strong velocity vectors also being parallel close to the shoreline. This already seen from the top-left panel of the figure, where bars are still relatively small compared to the other case. The shore-parallel currents are also called feeder currents. This result follows from the previous chapter (Fig.(4.5)), but now the circulating pattern is stronger (not shown). The relation with the morphological pattern is more clear from the bottom panel of the same figure, because the crescentic bars have almost reached their full growth and final shape. In general, the flow is directed shoreward over the crests, gets deflected in the form of feeder currents which then turn offshore as they pass through the channels.

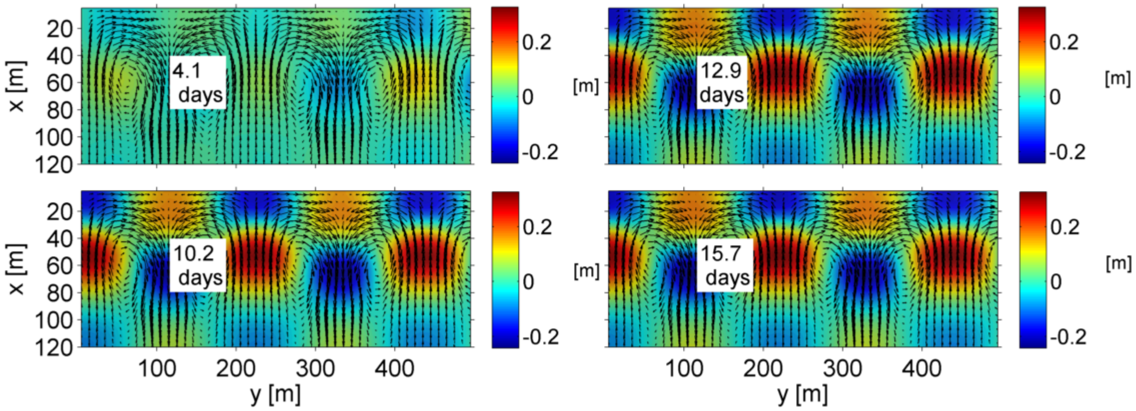

Figure 5.4: Snapshots of the bottom perturbations during different stages of their formation in the nonlinear regime ($t = 4.1, 10.2, 12.9, 15.7$ days). Contours show bottom perturbations h: red colour indicates crests and blue colour indicates troughs. The associated circulation, indicated by the vectors, is superimposed on the figure.

The magnitude of the inshore and offshore directed flow does not change significantly between $t = 4.1$ days and the final state. Rip current velocities are almost equal to the velocities over the shoals, although the former are a little larger. This agrees with previous studies on rip channel systems that highlight the difference: rip currents are more intense than currents over the crests as, also, rip channels are narrower than the crests. Nevertheless, their difference is small for the default case: $u_{\text{max,channel}} = 0.27 \text{ ms}^{-1}$ and $u_{\text{max,shoal}} = -0.22 \text{ ms}^{-1}$.

Moreover, the same procedure but for a roller-off case is followed. The final state of the bathymetry at $t = 15.7$ days and the evolution of the maximum amplitude A_m are shown in Fig.(5.5). Here, most of the bar growth occurs between $t = 0 - 3$ days. By that time sand bars grow up to $A_m = 0.42$ m at day 3.5. This is the maximum value that the bars reach for the entire run. From this day and until $t = 10.2$ days the amplitude decreases 0.06 m ($A_m = 0.36$ at that time). Then, remains almost constant until the end of the simulation, at $t = 15.7$ days.

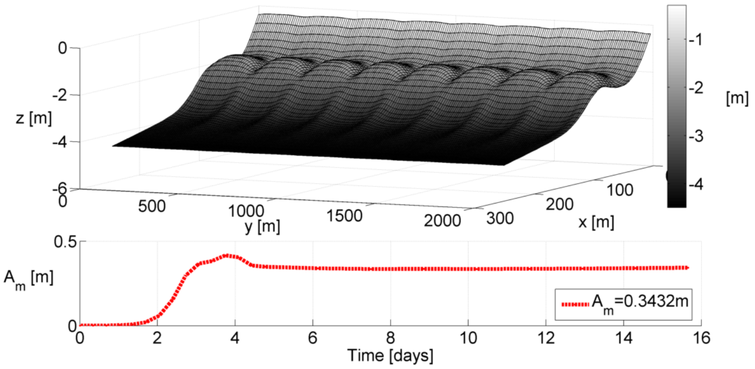

Figure 5.5: As in Fig.(5.1), but for the roller-off case.

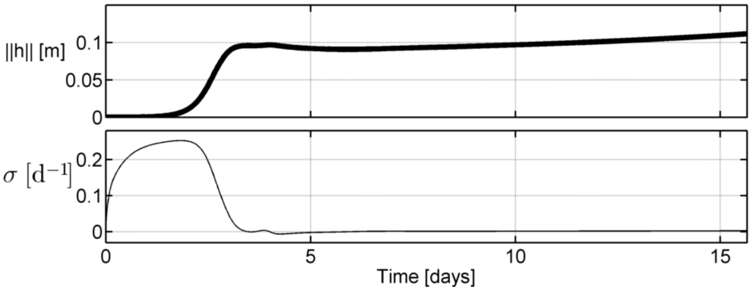

Figure 5.6: As in Fig.(5.2), but for the roller-off case.

As in the default case, the time when bars reach the finite amplitude regime and eventually stop growing is shown in Fig.(5.6). The onset of the nonlinear regime begins earlier than before. Following the criterion of negligible growth rate ($\sigma \simeq 0$) of Garnier et al. (2008) the system seems to result into a so-called saturated state after $t \sim 6$ days. Furthermore, four differences with respect to results of the default case should be stressed. First, the growing of bars is faster and the finite-amplitude regime is reached in just $t \simeq 2$ days, according to the bottom panel of Fig.(5.6) and the subsequent decrease of σ. Second, the overall growth rates are larger, with a maximum value of 0.26 d^{-1}. Third, σ appears to have negative values, which explains the decrease of the amplitude that was observed after 4 days in Fig.(5.5). Last, the growth rate has a tendency to increase after the saturation occurs, which is more evident from the profile of $||h||$ from the top panel of Fig.(5.6). Indeed, for an increase of $||h|| = 0.1 - 0.11$ m between $t = 13.7 - 15.7$ days then $\sigma \simeq 0.004$ d^{-1}, according to equation (3.7).

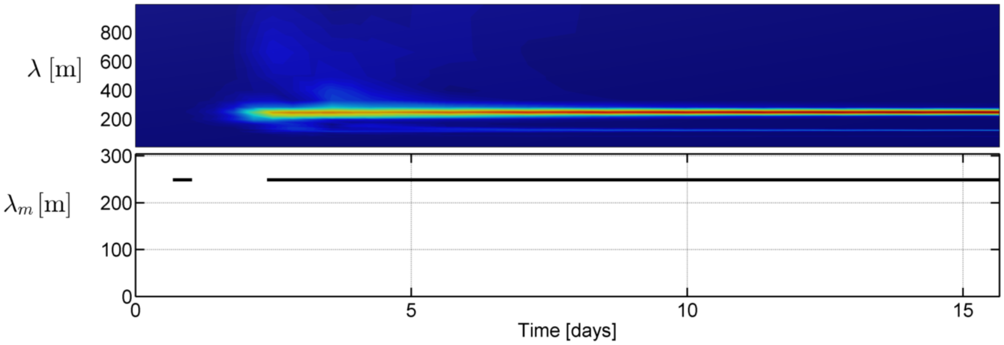

Figure 5.7: As in Fig.(5.3), but for the roller-off case.

From the top panel of Fig.(5.7) the results of performing a Fourier analysis on the bed perturbations $h(y, x_0, t)$ are shown for the roller-off case. For $t \simeq 2.5 - 7$ days there is a wider range of wavelengths compared to the analysis of the default case, indicating that more modes are active in the saturation process. The dominant mode has a wavelength of 250 m (bottom panel in Fig.5.7). For the rest of the simulation, i.e. after 7 days, the range of wavelengths is narrower and centered mostly around 250 m, a value which is larger than the default case.

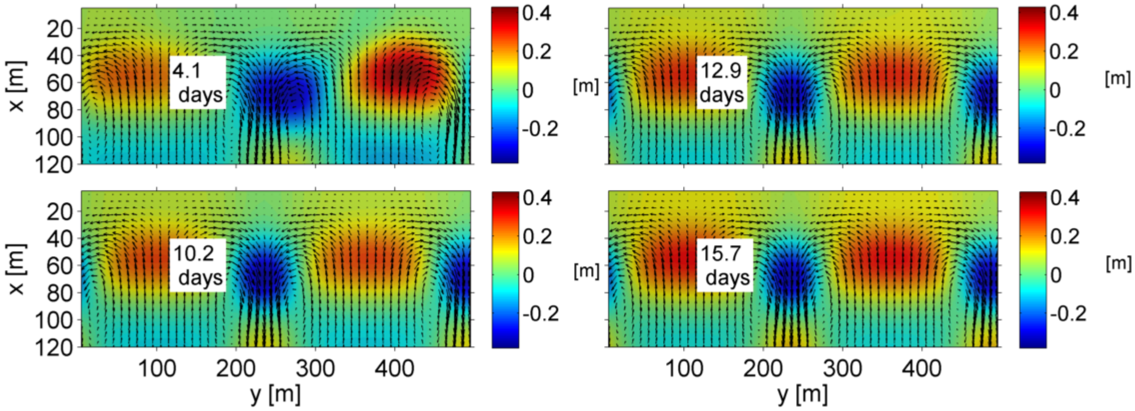

Figure 5.8: As in Fig.(5.4) but for the roller-off case.

In Fig.(5.8) the focus is on changes in the shape and the position of the patterns. This plot is similar to Fig.(5.4) but for the rollers off case. In this case, classical crescentic bars form, similar to those found by Calvete et al., (2005) with the main pattern line located at $x \simeq 60$ m. In this case, there is no evidence of any bar sequence at the shoreline (Fig. (5.8)). There is a bar line offshore of the longshore bar, at $x \simeq 120$ m, which is more pronounced at $t = 4.1$ days (top left panel), but then it slowly fades out. Crests becoming bigger and its troughs being smoothed out until $t = 15.7$ days. Crests and troughs of the main sequence ($x \simeq 60$ m) are more elongated in the longshore direction at the first snapshot (top left panel) and they become shorter as time goes by. Note, that in the default case there was a separate bar line between the main bar line at $x \simeq 60$ m and the shoreline during almost the entire run. Here, no such pattern is observed. Moreover, the crescentic pattern is associated with a certain flow circulation (Fig. 5.8). The corresponding flow is superimposed on the bottom perturbations on this figure. The difference between the maximum shoal velocity and the maximum channel velocity is $u_{\text{max,channel}} = 0.49\ \text{ms}^{-1}$and $u_{\text{max,shoal}} = -0.20$ m. The jet like character of the rip currents is observed on the red contours in Fig.(5.8). Compared to the previous case, rip currents are stronger and channels are narrower.

5.2 Mean sea level, energy and depth-integrated concentration

Increased wave breaking over the shoals leads to increased set up at these locations (Fig.(5.9)) for the default case (top left panel) and for the roller-off case (bottom left panel). These changes in the perturbed sea level z_{sper} drive a certain rip current current circulation (represented by the vectors). It is interesting that the set up is five times larger for the default case (rollers on) compared to the roller-off case very close to the shore ($x < 15$ m). For the former case it is also alongshore periodic in this region, whereas for the roller-off case this is not observed.

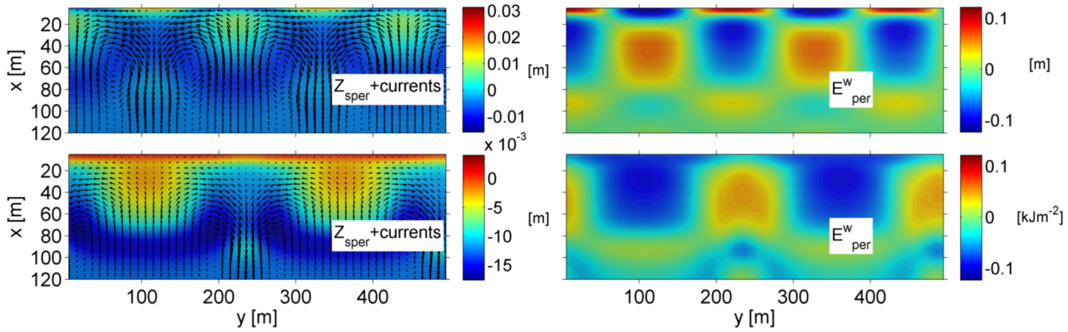

Figure 5.9: Left panels: Perturbed mean sea level z_{sper} for the default case (top) and the roller-off case (bottom). Vectors represent the currents. Right panels: Perturbed wave energy $E^{w'}_{per}$ for the default case (top) and the roller-off case (bottom). Snapshots are after $t = 12.5$ days of beach evolution.

Differences in the perturbed wave energy E^w_{per} are also clear: a different pattern is shaped for the default case with large positive and negative values almost at the shoreline (top right panel in Fig.(5.9)). On the other hand, for the rolller-off case E^w_{per} is alongshore periodic only at $x \simeq 70$ m. Following from Chapter 4 (Fig.(4.8)) the perturbed energy E^r_{per} (Fig.(5.10)) is in anti-phase with E^w_{per} for the default case. This means that where E^r_{per} is negative (positive) E^w_{per} is positive (negative).

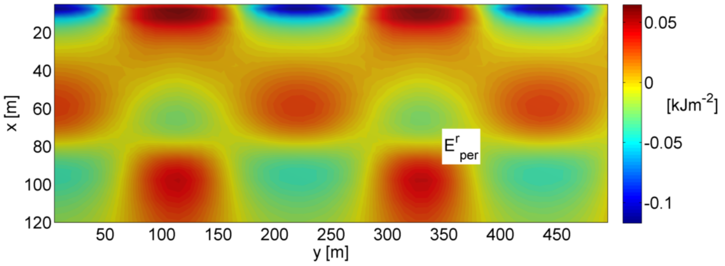

Figure 5.10: Perturbed roller energy E^r_{per} after $t = 12.5$ days.

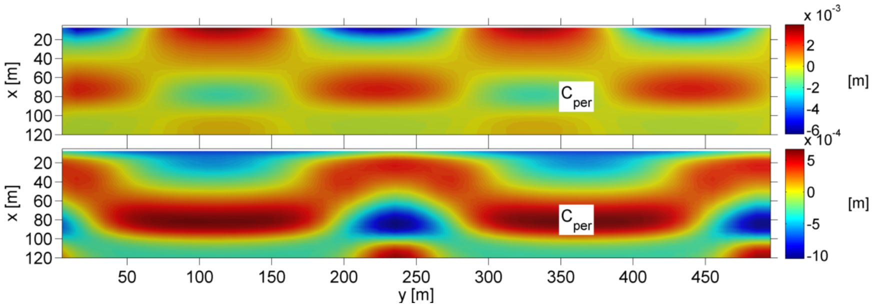

Figure 5.11: Top: Perturbed depth-integrated concentration C_{per} for the default case after $t = 12.5$ days. Bottom: As in the top panel, but for the roller-off case.

Perturbed depth integrated concentration C_{per} is related with sediment transport which is related with the evolution of the bottom. In Fig.(5.11) (top panel) longshore variations of C_{per} are evident very close to the shoreline when rollers are activated (default case). These variations are shifted offshore for the roller-off case (bottom panel). The magnitude in the values of C_{per} is almost ten times larger after $t = 12.5$ days for the default case compared to the roller-off case. This difference was not observed in the linear regime (4.9).

5.3 Wavelength, merging and splitting

Time series of the bottom perturbations reveal aspects of the nonlinear behaviour of patterns, such as merging or splitting of crests in time, possible migration and changes in the bar/channel dimensions. In (Fig.5.12) a time series is shown at the cross-shore location $x_0 = 52.5$ m. The formation of the crescentic patterns is initiated at the middle of the domain. The patterns, contained in $y = 800 - 1300$ m, seem to grow first and faster as they reach the finite amplitude regime at $t \simeq 3 - 4$ days with amplitudes of $A_m = 0.27$ m. On the other hand, the bars at the two sides of the domain grow slower and until $t = 5$ days have not reached yet such values. Notice that this figure is mostly representative of the main crescentic bar line ($x \simeq 60$ m). The two sand bars at the edges of the domain grow slower than the others. The spacing between them decreases between $t \simeq 4$ days and $t \simeq 7$ days. After $t > 4$ days there are $N_{\text{bar}} = 9$ crests, which means that the observed wavelength is $\lambda = L_y/N_{\mathrm{bar}} \simeq 222$ m, remaining the same during the entire simulation.

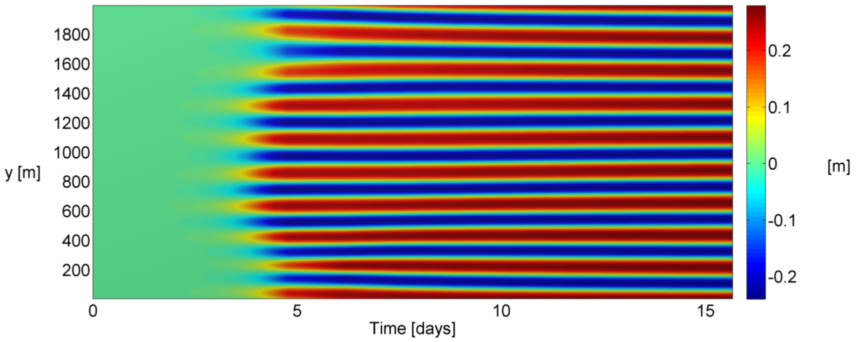

Figure 5.12: Contour plots of the time evolution of bed perturbations h at $x = 52.5$ m until $t = 15.7$ days and in plan view. Red colour is for the crests and blue is for the troughs. Results are for the default case.

For the roller-off case the time series of the bar formation at $x = 52.5$ m reveals the evolution of the bars during the different stages of their formation (Fig. 5.13). Here, the perturbations grow in a different way compared to that in the default case. Their amplitude becomes significant (deep yellow contours, $A_m = 0.2\,\mathrm{m}$) after $t \simeq 2.5$ days, whereas in the default case most of the bars had not reached such amplitudes before $t \simeq 3.7$ days (see Fig. 5.12). The first bars to grow are not the ones in the middle of the domain, but the ones on the edges ($x > 1600\,\mathrm{m}$ and $x < 500\,\mathrm{m}$).

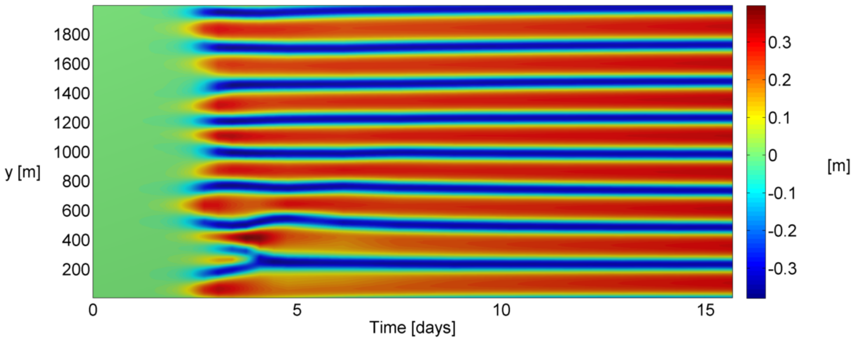

Figure 5.13: Same as in Fig.(5.12) but for the rollers off case.

Some of the patterns have the tendency to split, merge and change their length, especially, as it can be seen in Fig.(5.13) from $t = 2$ to 5 days. The biggest merging event happens in the bottom part of the domain ($x < 550$ m). Between 2.5 and 4.5 days, there are two channels that form (blue colour) that later merge into one after 4 days.

Chapter 6

Discussion

6.1 Formation of sand bars

Following previous studies (Falques et al., 2000 & Calvete et al., 2005), in this study it is shown that classical crescentic bars (without the rollers) rise as a free instability of the system and grow due to the positive feedback between the bed and the flow. In other words, the increased wave breaking over the crests is leading to changes in the mean sea level z_s that are alongshore periodic. In turn, a cellular current field is generated that accumulates sediment over the shoals, reinforcing them and, thus, creating a positive feedback. The accretion of sediment over the crests occurs in combination with a certain spatial distribution of the stirring of the sediment by the waves. This is understood if a bottom evolution equation is derived (Appendix B), i.e.

$$(1-p)\,\frac{\partial h}{\partial t} = \nabla\cdot(\Gamma\nabla h) - D\,\boldsymbol{v}\cdot\nabla\left(\frac{C}{D}\right). \tag{6.1}$$

According to this, accretion ($\partial h/\partial t > 0$) is induced when $\boldsymbol{v}\cdot\nabla\left(\frac{C}{D}\right) < 0$. This means that the component of the current $\boldsymbol{v}$ and the gradient of the depth averaged sediment concentration ($C_{da} = C/D$) have to oppose each other for accretion to occur. Indeed, this is what happens over the crests of the crescentic bars without the rollers. Fig.(6.1) shows the distribution of C_{da} after 12.5 days for this case. Combining this with the currents in Fig.(5.8), it is clear that the joint action of the onshore directed current at $y \simeq 100$ m and the steep offshore directed gradient of C_{da} across this location, leads to accumulation of sediment over the crest that is formed there. In a similar way, due to the offshore directed currents and the distribution of C_{da} in the channels, the latter are eroded further on. At the same time, sediment is accumulated offshore of the channel, thus creating a mirrored pattern (crests are followed by troughs offshore).

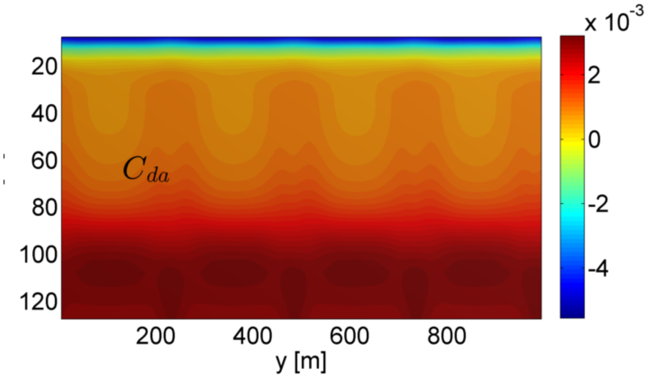

Figure 6.1: Depth averaged sediment concnetration $C_{da}(= C/D)$ after t = 12.5 days without rollers.

For the default case, the the principle is the similar (Fig.(6.2). The gradients are positive over the crests (offshore directed) and thus the shoals are reinforced by advection sediment by the currents that are directed onshore. In the inner surf zone the distribution of C_{da} is somehow different, as its alongshore periodicity, leads to a modified accretion pattern compared to the roller-off case, giving rise to shoreline sand bars.

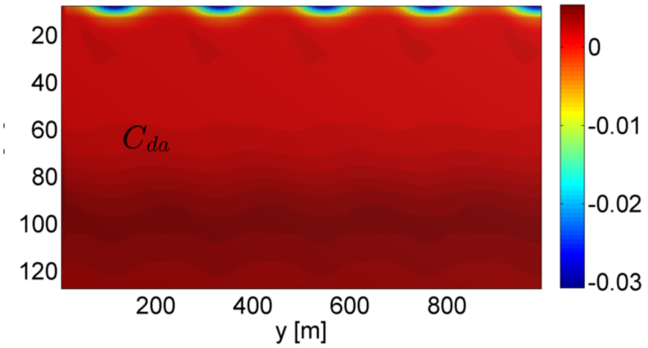

Figure 6.2: As in Fig.(6.1), but for the default case.

6.2 Sand bars at the shoreline: FOT run

Why do sand bars form in the inner surf zone with rollers? Which processes are mainly responsible for the observed changes in these bar characteristics? The possible candidates are found by inspecting in which ways the rollers are included in the model:

1. Additional forcing in the hydrodynamics, i.e. in the momentum balance, eq.(2.18), due to convergence of the roller radiation stresses (Option 1). This causes changes in the currents $\mathbf{v}$, the sediment transport $\mathbf{q}$ and the bed level z_b.
2. Different forcing in the currents by computing the lateral mixing coefficient, eq.(2.21), with D^r, instead of D^w (Option 2). This causes changes in the same variables as in 1.
3. Additional stirring of sediment, eq.(2.31), caused by the roller turbulent bores (Option 3). This causes changes in the sediment transport $\mathbf{q}$ and the bed level z_b.
4. A combination of options 1, 2 and 3, i.e. the default case configuration.

To further investigate on this, a new experiment is performed, namely the flow over topography (FOT) run. In the present case, it boils down into inspecting how the flow induced by these different drivers behaves over the topography of a fully formed crescentic bar pattern. First, a simulation without rollers is performed and the beach morphology evolves for several days. At a certain time, after the finite-amplitude regime is reached, configurations with cases 1 or 4 are activated. This way, the currents, which are now induced by both the waves and the rollers, are flowing over a topography that is not in principle compatible. Note that, hereafter experiments with settings of cases 2 and 3 are not performed. Case 2 is found to have very small impact on driving the currents, as the convergence of the Reynolds stresses is at least one order of magnitude smaller than the ones of the wave and the roller radiation stresses (not shown). Case 3 is considered to be physically unrealistic, as it is unlikely that turbulent bores could naturally exist without the inclusion of the rollers in the hydrodynamics. Finally, case 1 will include D^r in the computation of equation (2.21) as well.

The rollers-off configuration is run and after 12.5 days the rollers are activated only in the hydrodynamics, i.e. case 1 with $n_{bor} = 0$ in eq.(2.31). After spinning up the system, the difference Δu_{rms} in the root mean square velocity after activating the case 1 settings, i.e. $u_{rms,case\,1}$, from the $u_{rms,off}$, i.e. the roller-off configuration u_{rms}, is plotted in plan view in Fig.(6.3). The largest value is very close to the shoreline, namely for $x < 5$ m. In the rest of the domain, there is no notable difference ($\Delta u_{rms} \simeq 0$ ms^{-1}). Variations in the mean sea level z_s are an important driver of the currents, as they generate differences in pressure. Hence, differences in this field, meaning different set up and set down in the surf zone, are mainly responsible for the formation of different circulation patterns between the rollers-off and the case 1 configurations. Here, $\Delta z_s = z_{s,case\,1} - z_{s,off}$ is shown in the right panel of Fig.(6.3). The largest negative values of Δz_s are observed near the shoreline and they are alongshore periodic. Also, $z_{s,case\,1}$ is larger than $z_{s,off}$ for $x \simeq 20$ m, although the difference is not that large.

The distribution of C plays a key role as it represents the sediment that is available to be transported by the currents, according to equation (2.23). The difference ΔC is shown in the left panel of Fig.(6.4). Overall, there are very small differences between the two configurations, with the largest values spotted offshore of the longshore bar (for $x > 90$ m). Near the coast, the small differences in ΔC are alongshore periodic. The difference in the currents, on the other hand (right panel in the same figure), is more clear. The presence of strong current perturbations close and parallel the shoreline, as well as circulation cells at $x \simeq 40$ m, indicate that the circulation pattern is different now that before activating the rollers in the hydrodynamics.

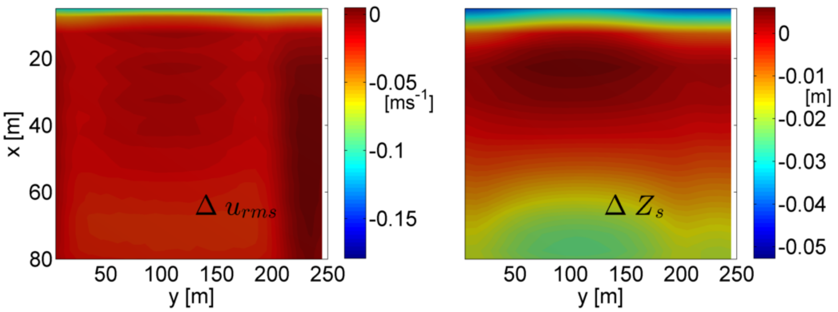

Figure 6.3: Left pannel: Difference $\Delta u_{rms} = u_{rms,case\,1} - u_{rms,off}$ of the root mean square velocity of the waves u_{rms} in the FOT run, after activating the rollers only in the hydrodynamics (case 1) and without any rollers (rollers-off). Right panel: as in the left panel, but for the mean sea level Z_s.

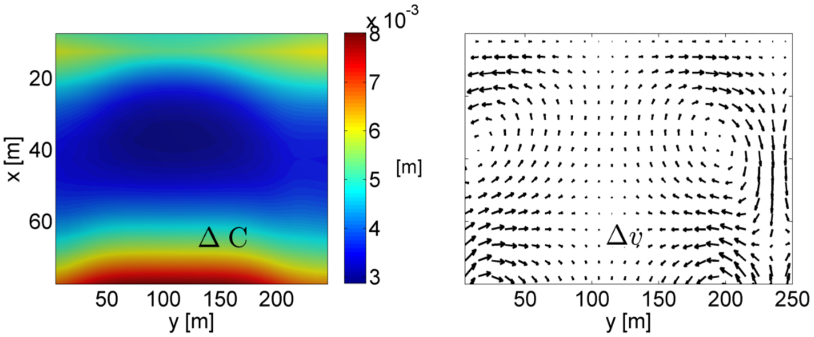

Figure 6.4: As in Fig.(6.3), but for the depth-integrated sediment concentration (left panel) and the current velocity field (right panel), represented by the arrows.

The latter is attributed to the difference in the forcing that is available to drive the circulation in the two cases. The study of Castelle at al. (2012) is followed and the mechanism that drives the currents is analyzed for each case of the FOT simulation, namely before and after switching on the case 1 configuration. The so-called residual forcing $\mathbf{F^{res}}$, comprising the vectorial sum of the pressure gradients $\mathbf{F^{p}}$ and of the radiation stress gradients of the waves $\mathbf{F^{w}}$ and the rollers $\mathbf{F^{rol}}$, reads

$$\mathbf{F^{res}} = \mathbf{F^{p}} + \mathbf{F^{w}} + \mathbf{F^{rol}} \tag{6.2}$$

or

$$\mathbf{F^{res}} = -\, g\frac{\partial z_s}{\partial x_i} - \frac{1}{\rho D}\frac{\partial}{\partial x_j}\left(S^w_{ij} + S^r_{ij}\right)\,,\ i,j = 1,2\,, \tag{6.3}$$

taken into account from the momentum balance, equation (2.18).

The difference ΔF^{res} is plotted in Fig.(6.5). This figure shows that, taking into account the modified mean set up due to the rollers in the hydrodynamics (right panel, Fig.(6.3)), which leads to a modified pressure gradient force (1st term in the rhs of equation (6.3), and the roller forcing, namely the convergence of the roller radiation stresses, shifts the maxima of the forcing closer to the shoreline. This is in agreement with the currents in the previous figure.

The negative divergence of sediment transport (right panel in Fig.(6.5)) determines the evolution of the bottom. It is related with the currents, via sediment transport relation (equation (2.23)). Interestingly, near the shoreline, strong divergence of sediment transport (green colour) is not observed where the feeder currents are. Nevertheless, the positive (negative) values of $-\vec{\nabla} \cdot \mathbf{q}$ agree with the currents behaviour. This is an indication that the joint action of the currents and the spatial distribution of C_{da} must be investigated. In Fig.(6.6), the pattern is similar to the one of Fig.(6.1). This is expected since the rollers are not included in the stirring of sediment ($n_{bor} = 0$). As it was shown in that case (previous section) the distribution of C_{da} (combined with the currents) tended to favor the formation of a specific crescentic bar system, that did not include sand bars at the shoreline. Therefore, in the present case, although the currents are much different than without the rollers, it is probable that sand bars will not form at the shoreline, due to the absence of a suitable C_{da} pattern.

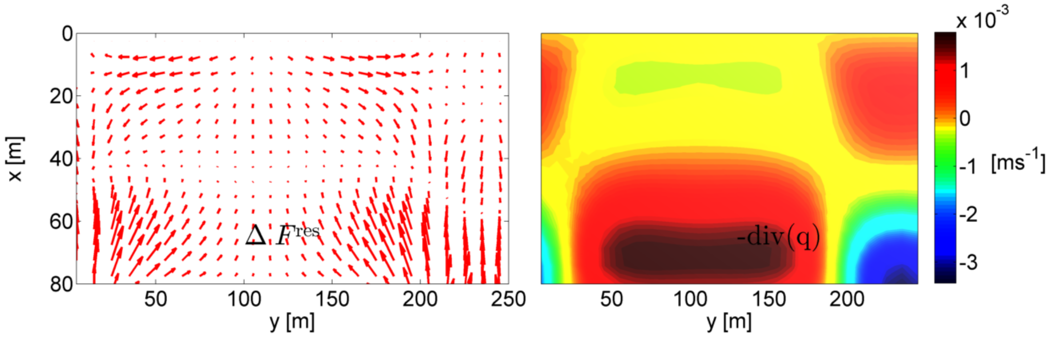

Figure 6.5: Left: Difference $\Delta F^{\mathrm{res}} = F^{\mathrm{res,a}} - F^{\mathrm{res,off}}$ of the residual forcing F^{res}. Right: minus the divergence of sediment transport $(-\vec{\nabla} \cdot \mathbf{q})$ after the rollers are "switched on" in the hydrodynamics. Blue-green colour indicates divergence of sediment transport and red colour convergence of sediment transport.

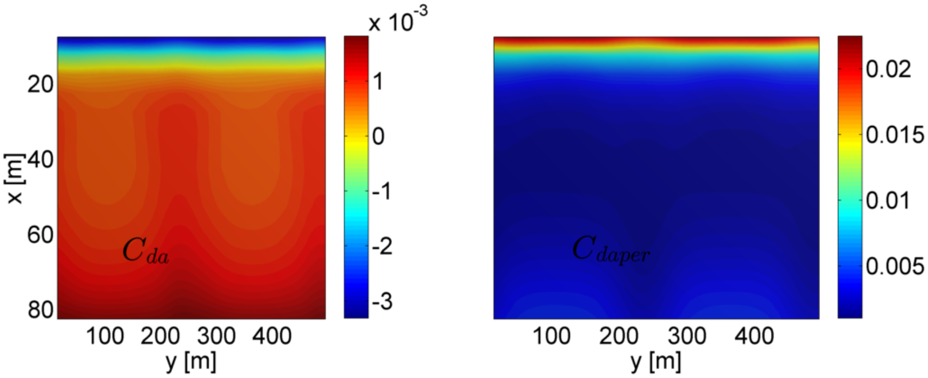

Figure 6.6: Left panel: Depth-averaged sediment concentrarion C_{da} for the FOT run and case 1. Right panel: The difference $\Delta C_{da} = C_{da,case\ 1} - C_{da,off}$.

For the second FOT run, the same procedure is followed, except that this time the rollers are included in both hydrodynamics and sediment transport (case 4). This means that $n_{bor} = 50$ in equation (2.31), as in the default case. As expected, the figures for the currents and the residual forcing show similar results as before, right panel in Fig.(6.7) and left panel in Fig.(6.8, respectively. The integrated sediment concentration, C on the other hand, has increased ten times in the inner surf zone compared to the case 1 FOT run, due to the inclusion of the roller turbulent bores in the stirring of the sediment. In Fig.(6.8), right panel, the divergence of sediment transport pattern shows strong erosion/deposition very close to the coast, in spite of the fact that the currents are the same in distribution and magnitude compared to the previous case (case 1). Analyzing of the bottom evolution equation, eq.(6.1), the C_{da} pattern, Fig.(6.9), reveals stronger cross-shore gradients of C_{da} in the inner surf zone than in case 1, which now allows for a different accretion/erosion pattern (combined with the currents behaviour). Also, it is shown (right panel in the same figure) that C_{da} shows larger and steeper longshore undulations compared to case 1 FOT run. The combination of the two characteristics, clearly favors the formation of crests and troughs in the inner surf zone, thus, concluding that a joint interaction of both rollers in the hydrodynamics and in the sediment transport is needed for shoreline bar patterns to occur.

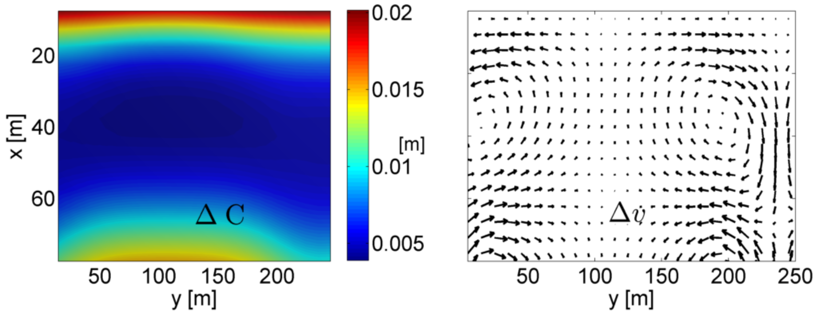

Figure 6.7: As in Fig.(6.4), but for the FOT run with the configuration of case d (all roller options activated).

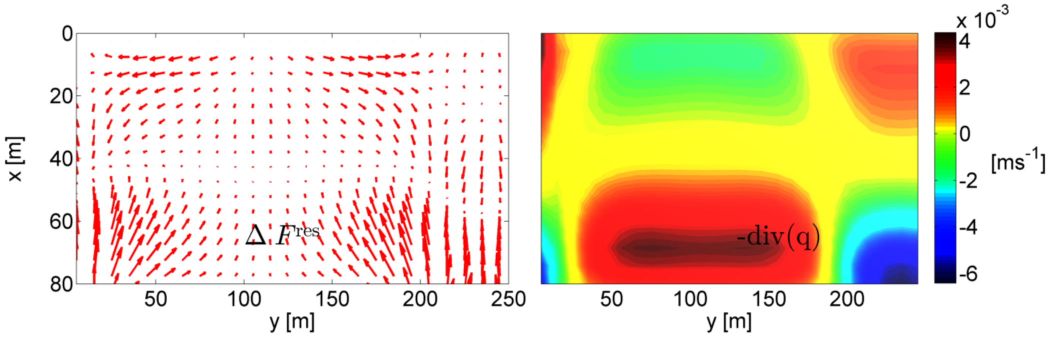

Figure 6.8: As in Fig.(6.5) but for the FOT run with configuration of case d.

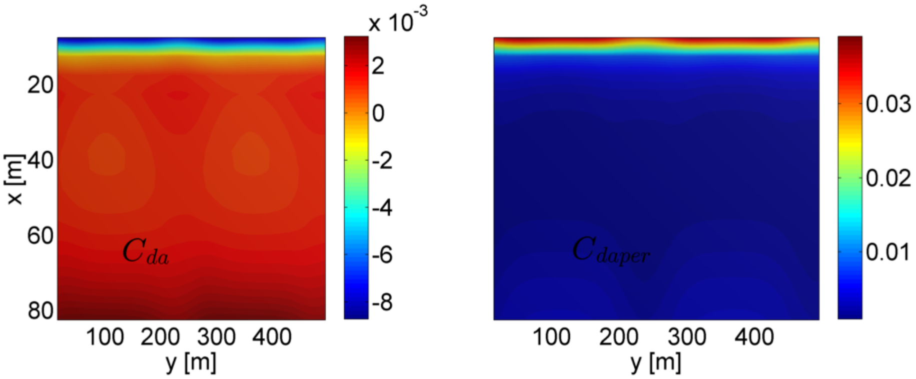

Figure 6.9: As in Fig.(6.6), but for the FOT run with all roller options activated (case 4).

6.3 Decrease of global growth rate

In Chapter 5, and following the study of Garnier et al. (2010), the finite amplitude regime of the bars was characterized by a saturation process ($\sigma \simeq 0$). In order to investigate the saturation process of the crescentic bars the global properties of the bed forms are analyzed. It boils down into analyzing the terms in the potential energy balance, which is derived by the modified bottom evolution equation (Appendix B). The potential energy balance is derived by multiplying the two sides of the BEE with the bottom perturbation h and by integrating over the whole domain (Garnier et al., 2006). It yields

$$\frac{\partial}{\partial t}\frac{1}{2}||h||^2 = P - \Delta \, , \tag{6.4}$$

with $||h||^2$ being the potential energy density of the bed forms. The first term in the rhs is the production of potential energy $\mathcal{P}$ due to advection of sediment transport, given by

$$P = -\overline{h\nabla \cdot (C\mathbf{v})} \simeq -\overline{hD\mathbf{v} \cdot \nabla C_{da}} \, , \tag{6.5}$$

where the overbar denotes averaging over the whole domain, given by equation (3.6). The second term is the loss of potential energy Δ due to the diffusive effect of downslope sediment transport and it reads

$$\Delta = -\overline{h\nabla \cdot (\Gamma \nabla h)} \, , \tag{6.6}$$

which is typically positive. By taking into consideration equation (3.7) the global growth rate is expressed as

$$\sigma = \frac{1}{||h||^2}\left(P - \Delta\right) \, . \tag{6.7}$$

According to this expression the bed forms grow if $P > \Delta$. Indeed, this is seen by the upper plot of Fig.(6.10).

Here, the two terms of the rhs of equation (6.4) are plotted as a function of $||h||$. It is interesting that only a slight difference between the production (blue line) and the damping terms (black line) of potential energy suffice for the bed instabilities to grow, which happens for $||h|| = 0.01 - 0.08$ m. For $||h|| \sim 0.08$ m the production $\mathcal{P}$ balances the loss Δ and the saturation point is reached for the first time, since $\sigma \simeq 0$ (expression (6.7). This corresponds to $t \simeq 5.5$ days in Fig.(5.2).

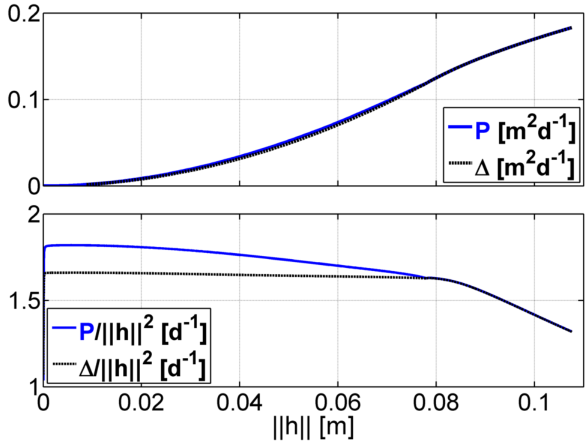

Figure 6.10: Top: Production term $\mathcal{P}$ (blue line) and damping term Δ (black line) versus $||h||$. Bottom: $\mathcal{P}/||h||^2$ (blue line) and $\Delta/||h||^2$ (black line) versus $||h||$. Both plots are for the default case.

This does not explain, though, why σ decreases and the instability mechanism saturates. In order to investigate that, the two terms of expression (6.7), i.e. $P/||h||^2$(blue) and $\Delta/||h||^2$ (black), versus $||h||$ are analyzed. According to the bottom plot of Fig.(6.10), the loss of potential energy (black line) is almost constant for $||h|| = 0-0.08$, which is the point where the saturation is first reached. According to this plot, the term that changes during the simulation is the production (blue line) and in particular it decreases until it balances Δ. In other words, sand bars seem to cease growing because the instability mechanism that first made them grow is weakened and not because the damping term is strengthened.

6.4 Limitations and suggestions for future research

The model was quite sensitive to several parameters, for instance to the change in waveheight at the offshore boundary H_{rms}^{off} and parameters such as the breaking index γ_b and the bedslope coefficient γ. For the first, simulations with Morfo55+ with rollers for values of H_{rms} below 1 m led to a stable bed profile with no sand bars growing. On the other hand, bars grew for the same waveheight and without rollers. For values above 2 m both cases were unstable after some time, meaning the sand bars were large enough to grow above the sea surface. The same happened in the case of $\gamma_b < 0.45$ or $\gamma < 3$, with the bars growing too much after a few days of beach evolution and never saturate.

An important success of this work is that it simulates the long term evolution of sand bars, first done by Garnier et al. (2008), both with the rollers and for a new experimental setting. For example, the friction formulation was different from Garnier et al. (2008). Also the wave/current interaction was implemented both in the energy and dispersion relation, something that the latter study did not account for. In that sense, the present study is more an extension of the previous work done by Ribas et al. (2012) rather than Garnier et al. (2008), despite the fact that the numerical model of the latter is used to simulate the long-term evolution of the bed features.

Last, an important extension of the present research would be to investigate the role of the surface rollers in the finite amplitude regime for oblique waves. Oblique waves are important to model because they are more frequently found in natural beach systems and therefore the corresponding simulations would somehow be more challenging. This would be the extension of the work of Ribas et al. (2012) who only analyzed the initial formation of bars in a model that included the surface rollers under oblique wave incidence. As it has been observed in the $\theta = 0^o$ scenario, in the finite-amplitude regime, there might be changes in λ and σ, thus strongly deviating from the results of linear stability analysis.

Chapter 7

Conclusions

In this project, for the first time, the long-term evolution of surf zone sand bars has been investigated with a nonlinear morphodynamic model that accounts for the effects of the surface rollers on their temporal and spatial characteristics. Normally incident waves were considered and a bottom profile with a shore-parallel bar. Systematic insight into the dynamics of bars was obtained by comparing and analyzing results between a default configuration, that included rollers, and a roller-off configuration. Also, with regard to the longshore averaged state and the initial formation of bars, model results were compared with those of other studies. First, the implementation of the rolller dynamics in the numerical model was successful, showing that the cross-shore profiles were numerically smooth. A comparison of the variables in the basic state showed that depth-integrated sediment concentration C is ten times larger compared to the roller-off case, due to the addition of the turbulent bore velocity of the rollers u_{bor} in the bed shear stress. Also, when rollers are included, maxima of C occur shoreward of the longshore parallel bar, compared to the roller-off case that the maxima are shifted offshore. A second peak of C is also observed very close to the coast. Interestingly, the maxima are shifted also for the mean sea level z_s and for the default case the set-up is smaller in the inner surf zone, than in the case without the rollers.

Furthermore, an analysis of the linear regime showed that sand bars in the two cases have different growth rates and spatial characteristics, meaning the wavelength, amplitude and shape. Analysis from global properties showed that, at this stage, $\sigma_{default} < \sigma_{rolloff}$ (0.15 d^{-1} and 0.25 d^{-1}, respectively). The corresponding e-folding time for the default case was 14 h and for the roller-off case 9.5 h. A comparison of results obtained from the the Morfo55+ model and the Morfo62 model, which is based on linear stability analysis, showed similar results for the default case. More specifically, growth rates obtained with either Fourier analysis or analysis of globally averaged properties were less than 5% different than the Morfo62 results. Therefore, the sand bars simulated with Morfo55+ were not represented by the fastest growing mode of the system. On the other hand, when rollers were de-activated the two models did not agree, i.e growth rates differ almost 50%. This can be attributed to inevitable configuration differences between the two models, e.g. the small difference in the wave height H_{rms}^{off} at the offshore boundary.

Long-term simulations of 15.7 days conducted with Morfo55+ revealed that shoreline undulations appear only when rollers are included in the model. For that case, a separate crest-trough-crest sequence is fully developing in the inner surf zone. When rollers are not activated this is not observed. For the latter case, the coupling between the bed and the flow gave rise to fully developed crescentic bar patterns. When rollers are activated differences are also observed in the wavelength and amplitude. When comparing results for the default case with those of rollers-off, the maximum amplitude is 0.29 m compared to 0.42 m . This value occurs in the final state, whereas for the latter occurs after $t = 4$ days. Crests are narrower and channels are wider. Also, the circulation characteristics are different: rip currents are almost two times weaker when rollers are accounted for.

It was found that the limit of the linear regime is reached after $\simeq 2$ days with rollers and after $\simeq 1.7$ days in the case of rollers-off. That's when the global growth rate σ starts to decrease and nonlinear effects become evident. Analysis of the growth rates for both cases indicated that bars grow, saturate and stabilize, according to $\sigma \simeq 0$, after several days. However, after $\simeq 13$ days bars start to grow again in the case without the rollers.

In order to gain further understanding about the changes in the bar characteristics caused by the rollers, two new experiments were performed (called the flow over topography runs). These runs isolated the processes of the rollers in the hydrodynamics and the sediment transport by inspecting how the different roller processes affect the evolution of the bed over a fully formed crescentic bar pattern. First, the rollers were included only in the hydrodynamics and second the rollers were fully included in the model. The bottom evolution equation was qualitatively analyzed in order to explain the erosion/accretion patterns. Although the currents were similar between the two cases, the difference in the depth-averaged concentration pattern when $n_{bor} \neq 0$, played a crucial role in the sediment deposition pattern very close to the shoreline. Therefore, it is concluded that shoreline sand bars tend to grow only if the roller processes are included in the sediment transport.

Conclusions on the effect of rollers in the long-term evolution of sand bars for other beach systems with different settings than the present one, should be carefully drawn. However, the settings used in this research project are commonly found in natural beach systems with a moderate wave climate, such as the beach at Duck, and certainly lie within the range of values that the observations indicate (Ribas et al. (2012)).

Appendix A

Bottom profile formulation

The initial topography $z_b(x, y, 0)$ follows,

$$z_b(x, y, 0) = z_{b0}(x) \ , \tag{A.1}$$

where the initial equilibrium profile $z_{b0}(x)$ reads,

$$z_{b0}(x) = -a_o - a_1 \left(1 - \frac{b_2}{b_1}\right) \tanh\left(\frac{b_1 x}{a_1}\right) - b_2 x + a_2 \exp\left[-5\left(\frac{x - x_b}{x_b}\right)^2\right] \ , \tag{A.2}$$

with x_b being the location of the longshore uniform bar crest (default case $x_b = 80$ m). The profile z_{b0} is supposed to represent the profile found in some natural coasts, such as the one in the coast at Duck, North Carolina. The rest of the parameters in equation (A.2) are: the height of the water depth at the shore boundary $a_0 = 0.25$ m, $a_1 = 2.97$ m and the bar amplitude $a_2 = 1.5$ m, . Finally, the shore and offshore slopes are $b_1 = 0.075$ and $b_2 = 0.0064$, respectively.

Appendix B

Bottom evolution equation (BEE)

A derivation of the bottom evolution equation (BEE from now on) following Garnier et al. (2006) is presented here. First, the conservation of sediment mass (2.22) and the sediment transport (2.23) equations are combined. This yields

$$(1-p)\,\frac{\partial h}{\partial t} + \nabla\cdot(C\boldsymbol{v}) - \nabla\cdot(\Gamma\nabla h) = 0\,, \tag{B.1}$$

with C representing the depth integrated sediment concentration, given by (2.21) and Γ being the bedslope coefficient, given by (2.30). Also $\partial z_b/\partial t = \partial h/\partial t$ since z_{bo} is constant in time. The second term in the lhs of (B.1) can be written as

$$\nabla\cdot(C\boldsymbol{v}) = \nabla\cdot\left(\frac{C}{D}D\boldsymbol{v}\right) = D\nabla\left(\frac{C}{D}\right)\cdot\boldsymbol{v} - \frac{C}{D}\frac{\partial D}{\partial t}\,, \tag{B.2}$$

where the water mass conservation (2.15) has also been used. By inserting (B.2) into (B.1) it follows

$$(1-p)\,\frac{\partial h}{\partial t} = \nabla\cdot(\Gamma\nabla h) - D\,\boldsymbol{v}\cdot\nabla\left(\frac{C}{D}\right) + \frac{C}{D}\frac{\partial D}{\partial t}\,, \tag{B.3}$$

Garnier et al. (2006) found that the last term in the rhs of equation ((B.3)), for the case that rollers are not included in the model, can be neglected for several reasons: First, for a current $|\boldsymbol{v}| \sim 1$ ms^{-1}and for assuming depth of $D \gtrsim 0.1\,\mathrm{m}$ an upper bound for C is obtained, yielding. $C \lesssim 10^{-3}\,\mathrm{m}$. Consequently, the depth averaged concentration $C_{da} = C/D \lesssim 10^{-2}$. Second, by assuming a quasi steady behaviour, i.e. that the flow adjusts instantaneously to the slow changes of the bed, $|\partial D/\partial t| = |\partial z_s/\partial t - \partial h/\partial t| \sim |\partial h/\partial t|$. Therefore the last term in the rhs of ((B.3)) is very small compared to the term on the lhs and can be neglected. Thus, the BEE reads

$$(1-p)\,\frac{\partial h}{\partial t} = \nabla\cdot(\Gamma\nabla h) - D\,\boldsymbol{v}\cdot\nabla\left(\frac{C}{D}\right)\,. \tag{B.4}$$

Bibliography

[1] Caballeria, M., Coco, G., Falques, A. and Huntley, D. A., 2002, Self-organization mechanisms for the formation of nearshore crescentic and transverse sand bars, *Journal of Fluid Mechanics*, vol. 465, pp. 379–410, DOI: 10.1017/S002211200200112X.

[2] Calvete, D., Dodd, N., Falques, A. and van Leeuwen, S.M., 2005, Morphological development of rip channel systems: normal and near-normal wave incidence, *Journal of Geophysical Research*, VOL. 110, C10006, doi:10.1029/2004JC002803.

[3] Calvete, D., Ribas, F. , De Swart, H. E. and Falques, A., 2011, Effect of surface rollers on the formation of crescentic bars, *River, Coastal and Esuarine Morphodynamics*, RCEM2011.

[4] Castelle, B., Marieu, V., Coco, G., Bonneton, P., Bruneau, N., Ruessink, B. G., On the impact of an offshore bathymetric anomaly on surf zone rip channels, *Journal of Geophysical Research*, VOL. 117, F01038, doi:10.1029/2011JF002141.

[5] Falques, A., Coco, G. and Huntley, D. A., A mechanism for the generation of wave-driven rhythmic patterns in the surf zone, *Journal of Geophysical Research*, VOL. 105, NO. C10, PAGES 24,071-24,087.

[6] Feddersen, F., Guza, R. T., Elgar, S. and Herbers, T.H.C., 2000, Velocity moments in alongshore bottom stress parameterizations, *Journal of Geophysical Research*, , VOL.105, NO.CA, PAGES 8673-86.

[7] Garnier, R., 2006, Nonlinear modeling of surf zone morphodynamical instabilities, PhD Thesis, *Appl. Physics Dept., Unv. Politecnica de Catalunya, Barcelona, Spain*

[8] Garnier, R., Calvete, D., Falques, A. and Dodd, N., 2008, Modeling the formation and the long-term behavior of rip channel systems from the deformation of a longshore bar, *Journal of Geophysical Research*, VOL. 113, C07053, doi:10.1029/2007JC004632.

[9] Garnier, R., Dodd, N., Falques, A. and Calvete, D., 2010, Mechanisms controlling crescentic bar amplitude, *Journal of Geophysical Research*, VOL. 115, F02007, doi:10.1029/2009JF001407.

[10] Horikawa, K., 1988, Nearshore dynamics and coastal processes, *University of Tokyo Press*

[11] Konicki, K. M., Holman, R. A., 2000, The statistics and kinematics of transverse sand bars on an open coast, *Marine Geology*, 169 (2000) 69–101.

[12] Lippmann, T. C. and Holman, R. A., 1990, The spatial and temporal variability of sand bar morphology, *Journal of Geophysical Research*, VOL. 95, NO. C7, PAGES 11, 575-11, 590

[13] Longuet-Higgins, M. S. and Stewart, R.W., 1964, Radiation stresses in water waves: a physical discussion with applications, *Deep Sea Research*, Vol. II, pp. 529 -562: Pergamon Press Ltd.

[14] Reniers, A. J. H. M., Roelvink, J.A. and Thornton, E.B., 2004, Morphodynamic modeling of an embayed beach under wave group forcing, *Journal of Geophysical Research*, VOL. 109, C01030, doi:10.1029/2002JC001586.

[15] Ribas, F., 2003, On the growing of nearshore sand bars as instabilities processes of the equilibrium beach states, PhD Thesis, *Appl. Physics Dept.*, *Unv. Politecnica de Catalunya*, *Barcelona*, *Spain*

[16] Ribas, F., de Swart, H. E., Calvete, D. and Falques, A., 2012, Modeling waves currents and sand bars on natural beaches: the effect of surface rollers, *Journal of Marine Systems*, 88, 90-101.

[17] Ribas, F., de Swart, H. E., Calvete, D. and Falques, A., 2011, Modeling and analyzing observed transverse sand bars in the surf zone, *Journal of Geophysical Research*, VOL. 117, F02013, doi:10.1029/2011JF002158.

[18] Ruessink, B. G., Miles, J. R., Feddersen, F., Guza, R.T. and Elgar, S., 2001, Modeling the along shore current on barred beaches, *Journal of Geophysical Research*, VOL. 106, NO. C10, PAGES 22, 451-22, 463.

[19] Short, A. D., 1999, Handbook of beach and shoreface morphodynamics, *Wiley Chichester*, pp.230-250.

[20] Soulsby, R. L., 1997, The dynamics of marine sands, *Thomas Telford*, *London*, *UK*.

[21] Thornton, E. B. and Guza, R. T., 1983, Transformation of wave height distribution, *Journal of Geophysical Research*, VOL. 88, NO. C10, PAGES 5925-5938.

[22] Wright, L. D. and Short, A. D., 1984, Morphodynamic variability of surf zones and beaches: a synthesis, *Marine Geology*, 56 (1984) 93–118.

[23] van Enchevort, I. M. J., Ruessink, B. G., Coco, G., Suzuki, K., Turner, I. L., Plant, N. G., and Holman, R. A., 2004, Observations of nearshore crescentic sand bars, *Journal of Geophysical Research*, VOL. 109, C06028, doi:10.1029/2003JC002214

[24] Yu, J. and Slinn, D., 2003, Effects of wave-current interaction on rip currents, *Journal of Geophysical Research*, VOL. 108, NO. C3, 3088, doi:10.1029/2001JC001105.